INTERPRETABLE FUSION ANALYTICS FRAMEWORK FOR fMRI CONNECTIVITY: SELF–ATTENTION MECHANISM AND LATENT SPACE ITEM–RESPONSE MODEL*

Jeong-Jae Kim[†]
Yonsei University
jeongjaekim@yonsei.ac.kr

Yeseul Jeon[†]
Yonsei University
jeon9677@yonsei.ac.kr

SuMin Yu
Duke University
sumin.yu@duke.edu

Junggu Choi
Yonsei University
junggu.choi@yonsei.ac.kr

Sanghoon Han[‡]
Yonsei University
sanghoon.han@yonsei.ac.kr

ABSTRACT

There have been several attempts to use deep learning based on brain fMRI signals to classify cognitive impairment diseases. However, deep learning is a hidden black box model that makes it difficult to interpret the process of classification. To address this issue, we propose a novel analytical framework that interprets the classification result from deep learning processes. We first derive the region of interest (ROI) functional connectivity network (FCN) by embedding functions based on their similar signal patterns. Then, using the self-attention equipped deep learning model, we classify diseases based on their FCN. Finally, in order to interpret the classification results, we employ a latent space item-response interaction network model to identify the significant functions that exhibit distinct connectivity patterns when compared to other diseases. The application of this proposed framework to the four types of cognitive impairment shows that our approach is valid for determining the significant ROI functions.

Keywords fMRI · ADNI · Functional Connectivity Network · Deep Learning · Latent Space Item-Response Model

Introduction

Recently, Deep Neural Networks (DNN) have emerged as popular models of computation in classifying the different cognitive impairment groups in neuroimaging research [1, 2]. However, when it comes to classifying diseases with functional magnetic resonance imaging (fMRI) data (i.e., time–series data in resting state fMRI), improving classification accuracy has proved to be challenging given that the brain dynamics captured are high–dimensional, and not readily interpretable due to the complexity of subject–specific temporal and spatial signals (i.e., spatial maps with associated time courses between nodes). As such, typical deep learning models consist of hidden black box structures, which makes the interpretation of how the model actually produced the output hard to interpret.

Previous studies have mainly focused on summarizing brain functions called Regions of Interests (ROIs) signals, comparing two ROI signal patterns by using methods such as Pearson correlation matrices [3] and Fisher transformation score [4]. Despite the fact that this approach offers valuable advantages, such as the ability to simply and intuitively capture the whole–brain interactions as proxy representation of networks, these comparisons of pairwise–(dis)similarities only considers conditional relationships by controlling for high degrees of correlation, such as triangular correlation [5]. By doing so, a lot of valuable information may be lost due to the relative simplicity of this approach.

---

[*]Under review

[†]Equal contribution

[‡]Corresponding author

The nature of fMRI data is inherently high–dimensional signal data that consists of three dimensions; patient group, time, and ROIs. Given that multivariate data may suffer from the curse of dimensionality, reducing dimensionality is inevitable; this step is crucial in order to facilitate the identification, analyses, and interpretation of the data, which are often done using a univariate feature selection procedure that considers neither the spatial structure of the data, nor the multivariate characteristics of the signal.

In order to avoid redundancy and noise while maintaining core latent features in the data to represent functional brain network with the goal of embedding brain functions to estimate their connections, we implemented several linear and non–linear dimensionality reduction techniques; Principal Component Analysis (PCA) [6], T–stochastic neighbor embedding (t–SNE) [7], Uniforma Manifold Approximation Projection (UMAP) [8]. t–SNE and UMAP model the manifold using stochastic (i.e., converting neighborhood's distance into conditional probability that represents similarity) and topological (i.e., fuzzy simplicial complex with edge weights representing the likelihood of connectivity) information, respectively. By using unsupervised and non-linear manifold learning to project ROIs onto spaces of lower dimensionality, t–SNE and UMAP preserves the distance and identities of probable neighborhood (i.e., ROIs, nodes). However, since dimension methods only return the latent position of ROIs, we must define connections between ROIs using their latent position on R2 space. To accomplish this, we used TDA's mapper [9] to implement partial clustering, which we then used to define connections. If some ROIs are assigned to the same cluster, those ROIs are assumed to be connected to one another. Similarly, we can apply this concept at the end to other partial clusters that define connections from local to global connections. We then built a FCN that captures all degrees of similarities between ROIs (Pearsons's r, Fisher Z–transformed, PCA, t–SNE, UMAP) and were interested in comparing the capabilities of the different dimension reduction methods for distinctively representing functional network patterns from one population to another.

In this study, our main aim was to identify the significant ROIs from each cognitive disease group that exhibits distinct signal patterns from other groups. We assume that if the FCN accurately represents the connections, the classification model based on each patient's FCN network returns are highly accurate. However, due to the dimensionality reduction, it is still difficult to validate their connections unless the data does not contain any labels, since it is an unsupervised learning approach. To combat these shortcoming, we came up with a novel analytical framework. We did this by adopting a classification model, self–attention equipped deep neural network, which can handle correlated structure data and train their adjacency connections well [10, 11, 12]. Attention Mechanism is used to focus on specific input values from sequence–based tasks that are most relevant to the input in order to reduce information loss and increase information power [13]. Our study, which focused on networks with ROIs correlations with inter–dependencies in its input sequences, used a self–attention mechanism that maximized local interactions by incorporating multi–head self–attention layers onto a deep neural network architecture. The similarity of two ROIs in an input sequence is captured by an attention score measuring the distance of their representations simultaneously attending to every ROI data including its own data. Self–attention estimates the interaction between input values and generates outputs that focus on reflecting the predicted interaction feature when the model performs predictions, classifications or other calculations. This self–attention deep model aids in the training of network information, not only for local connections but also for global connections. If the accuracy is sufficient, the output is a reliable source to decipher what brain functions or connectivity distinguishes the different disease population pairs.

The self–attention deep model not only improves prediction accuracy, but it also produces the ROIs attention distribution of each patient. The attention distribution of the ROIs indicates how the self–attention deep model trains the correlated structured input data; each ROI in the attention distribution defines the likelihood of how one specific ROI relates to other ROIs, producing a representation of every ROI and the weights among different ROIs. Fig. 3 depicts the scalar weight, a weighted sum indicating the relation between one ROI point to all other points. The learned attentional representation is subsequently fed through a softmax layer for normalization of the neighborhood, in order to train an end–to–end deep learning model and to obtain the map of attention weights. We can then use self–attention deep model to summarize the FCN connectivity into ROI attention distribution and infer how the deep learning model arrived at that classification decision based on the output of the ROIs attention distribution. As a result, the self–attention deep model is more efficient than other deep learning models in terms of interpreting the model's process through the output of attention distribution.

In terms of classification result interpretation, one of the most efficient statistical methods for handling correlated structure is network analysis. This network visualizes the relationship of ROIs in an intuitive way and allows us to directly inspect significant network features that represent a specific group over different pairs of disease populations. Specifically, network modeling estimates the relationships of interactions among nodes based on their dependency structure. It can provide global and local representation of nodes simultaneously. By visual scanning of latent position of each ROI, we can distinguish particular ROIs that share connectivities with other regions (i.e., more likely to be located in the center on the latent interaction map) from specific ROIs that are unique and independent (i.e. located

relatively away from the center of interaction map); by this visualization, we can figure out which ROIs contribute to the classification of the different disease groups.

We estimated and visualized the ROIs relationships using the Latent Space Item Response Model (LSIRM) [14]. This was done by mapping unobserved interactions among regions onto the interaction map based on the latent distance regions, where the interactions among ROIs are quantified from the weight representation output of the self–attention deep model. The LSIRM views binary item response data as bipartite network data that estimates the relationships between respondents(patients) and items(ROIs). This model measures the distances between the respondents(patients) and items(ROIs) as a penalty term in order to model the respondents' probabilities of giving the correct (or positive) responses. Here, the respondent–item distances represent their relations given the respective main effects. Since, we our classification result is regarded as continuous item response data, we adopted continuous version of LSIRM [15]. The between–regions distances indicate interactions in the network of interest, where shorter distances indicate stronger between–regions connections.

The LSIRM model can quantify closeness between ROIs by reflecting degrees of similarities. We were able to select the significant ROIs of each disease group that were unique to that particular group by using a statistical network model. This way, were able to focus on a selected subset significant ROIs to see what regions were important to focus on in the order to gain insight into understanding the different characteristics of the disease groups. The subsequent section will go over our findings from our analytical framework in greater detail.

We sought to validate the feasibility of application of the proposed fusion deep learning analytics framework by classifying resting state–fMRI (rs–fMRI) data for neurodegenerative diseases in different stages. There are different levels of cognitive impairment, characterized by the severity brain function impairment. We used resting brain scans provided by Alzheimer's disease Neuroimaging Initiative (ADNI) database, a representative multisite longitudinal study that has been used in various studies [16] [17] for exploring biomarkers for AD diagnosis. Since over a thousand publications have used the ADNI data, it allows us to examine if the current methods in our work produce meaningful features consistent with previous findings in addition to discovery of latent functional ROI groups.

Results

A novel analytical framework for determining the ROIs features that differentiate between diseases

In this study, we aim to model an approach that helps highlight an decipher the distinct ROIs that distinguishes two different diseases, such as Alzheimer's Disease (AD) vs. Mild Cognitive Impairment (MCI), AD vs. Early MCI (EMCI), AD vs. Late MCI (LMCI), and EMCI vs. LMCI. Our framework is shown in Fig. 1. Our method consists of three steps: (1) building a FCN using five different methods to represent community information, (2) developing a self–attention classification deep model for disease pairs, and (3) developing a network model for extracting meaningful features based on attention–distribution.

Step1: ROI connectivity network of diseases to figure out the interaction structure

In the first step, we built a FCN among regions based on their rs–fMRI Blood–Oxygen–Level–Dependent (BOLD) signals to figure out the correlated relationships between ROIs, which encompasses the unique characteristics of each particular disease. We extracted the 116 rs-fMRI BOLD signals using automated anatomical labeling(AAL)-116 template [18]. Table 2 describes AAL-116 templates. Fig. 2 shows the ROIs, rs–fMRI BOLD signal and the resulting 5 unique FCN graphs for sample LMCI patients (see Appendix A for the FCN graphs from other disease groups. First, subfield (a) of each figure represents the rs–fMRI BOLD signal for patients within the disease group showing much fluctuations within the majority of the ROI BOLD signals even during resting state as well as the intricacies of the inter–connectivity within these ROIs. Past research has used Pearson's r or Fisher's z values to generate FCN, which is shown in (b) and (c) of each figure. These correlation–based FCNs are intricately interconnected. It is difficult to properly comprehend the special attributes present in each area.

In order to decipher the relationship between the heavily interconnected brain regions, this study administered the brain regions into latent spaces in order to estimate the latent position between brain regions. Fig. 2 (d) shows the results of brain region patterns embedded in 2 axes with the highest exploratory power. This was calculated by utilizing PCA which is based in linear space. This was done by distributing the ROIs in a euclidean space and evaluating how the ROIs are positioned within the latent space. The final FCN based through PCA (linear space–based FCN) was constructed by using the Mapper's partial clustering method, which determines that ROIs are connected if they were clustered to the same group. Fig. 2 (e) utilized the t–SNE(stochastic space–based FCN), which embedded the relationship between the different brain regions into a latent space. This method assumes that the patterns between the brain regions are a specific probability distribution and learns the degree of similarity between these different distributions. Fig. 2 (f)
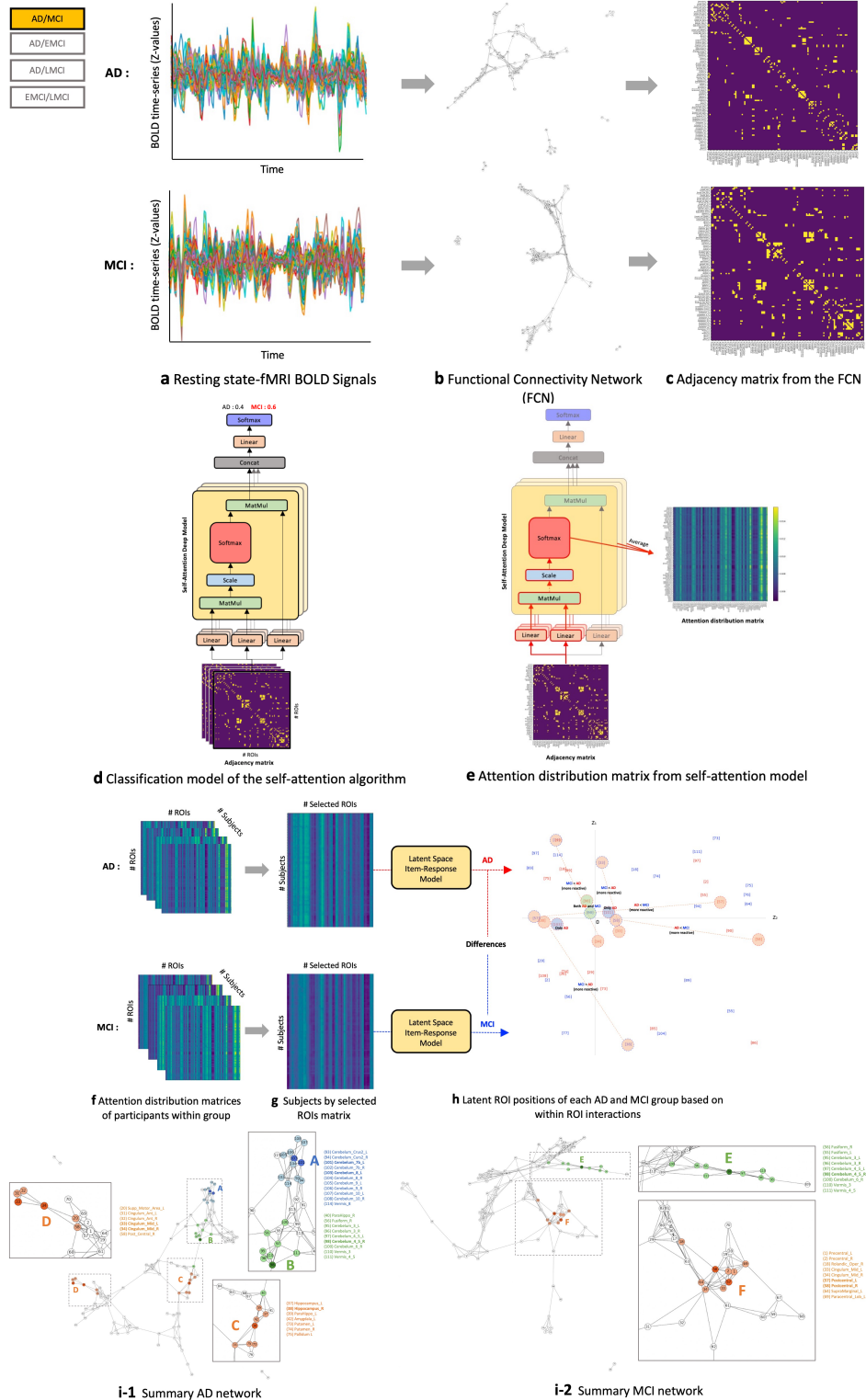
Figure 1: **Illustration of the proposed approach** Step 1: Construct Functional Connectivity Network(FCN;**b**) from resting state-fMRI BOLD signals (**a**) using five different methods: (1) Pearson's r score, (2) Fisher's z score, (3) PCA, (4) t-SNE, and (5) UMAP. Extract adjacency matrix(**c**) from FCN. Step 2: Implement binary classification model(**d**) to two pairs of diseases based on adjacency matrix of each disease and extract attention distribution matrix from self-attention model(**e**). Export the attention distribution matrices of participants in each group(**f**) and select meaningful ROIs(**g**). Step 3: Using the latent space item response model, estimate relationships between ROIs based on their latent positions(**h**) and summarize each disease group using meaningful ROIs that distinguish between the diseases(**i**).

4

used UMAP (topological space–based FCN) whose key benefit to capture how topologically similar the waveforms of bold signals generated by the ROIs are. By assuming a variety of different latent spaces, we are able to view the complicated web of ROIs connectivity from multiple different perspectives, which enables us to understand the structure of ROIs characteristics. In this study, we used the aforementioned FCN generated in 5 different ways as the input for the classification model that classifies the disease pairs in step 2.

Step2: Binary Classification model based on ROI connectivity network

If disease classification done through each patient's FCN is successful, the meaningful features of ROIs from FCN that were utilized to determine this classification can be said to be representing specific and distinct characteristics of the disease. This study used the self–attention deep learning to carry out disease classification through FCN where there exists dependency between data. This model trains the overall relationship between the different observations and their local relationship for each unique observation, which has the advantage of being able to learn the dependency structure of the data well. Furthermore, it is also possible to obtain the map of attention weights of the ROIs representing how the specific patterns of FCN connectivity have contributed to successful classification decisions.

Table 1 shows the performance of the self–attention deep model. When compared the classification performance to the recent studies [19, 20] and the baseline models [21, 22, 23]) (i.e.,eXtreme Gradient Boosting, Multi Layer Perceptron, Convolutional Neural Networks), our method outperforms in all disease group pairs. Noticeably, the stochastic based and topological based FCN, representing the hidden connectivity among ROIs, yielded the highest accuracy among disease group pairs reflecting the superiority of utilizing high dimensional dependency ROI structure.

Method	AD/MCI	EMCI/AD	LMCI/AD	EMCI/LMCI
[19]	0.8890	-	-	-
[20]	-	0.7920	0.6520	0.6090
PEARSON+XGBoost	0.7949	0.8206	0.8511	0.7802
FISHER+XGBoost	0.7460	0.6254	0.6353	0.6776
PEARSON+MLP	0.8132	0.7600	0.7809	0.7457
FISHER+MLP	0.7835	0.7533	0.7900	0.7605
LINEAR+MLP	0.7461	0.7333	0.7146	0.7452
STOCHASTIC+MLP	0.7659	0.7600	0.6427	0.7381
TOPOLOGICAL+MLP	0.7819	0.7067	0.6518	0.6838
PEARSON+CNN	0.8654	0.7733	0.7355	0.7667
FISHER+CNN	0.8648	0.7390	0.7809	0.7267
LINEAR+CNN	0.7747	0.7586	0.7891	0.7600
STOCHASTIC+CNN	0.8176	0.7657	0.7246	0.8200
TOPOLOGICAL+CNN	0.8192	0.7600	0.7155	0.7600
PEARSON+Self–Attn	0.8659	0.8067	0.8809	0.8071
FISHER+Self–Attn	0.8813	0.8133	0.8718	0.8152
LINEAR+Self–Attn	0.9022	0.8467	0.8627	0.8624
STOCHASTIC+Self–Attn	0.9033	**0.8867**	0.8900	**0.8971**
TOPOLOGICAL+Self–Attn	**0.9104**	0.8733	**0.9173**	0.8695

Table 1: Table 1 shows the performance of our self–attention deep model. When compared to the baseline model, our method outperforms in all disease group pairs.(XGBoost: eXreme Gradient Boosting [21], MLP: Multi Layer Perceptron [22], CNN: Convolutional Neural Networks [23], Self–Attn: Self–Attention Deep Model, PEARSON: Pearson's r–based FCN, FISHER: Fisher's z–based FCN, LINEAR: Linear space–based FCN, STOCHASTIC: Stochastic space–based FCN, TOPOLOGICAL: Topological space–based FCN)

Through the self–attention deep model, we obtain the attention distribution $\mathbf{W}_{p,(i,j)} \in \mathbf{R}^{4\times116\times116}, p = \{AD, MCI, EMCI, LMCI\}, (i,j) = \{1,\cdots,116\}$. From each pair of diseases, there are 116 number of attention distribution matrix $\mathbf{W}_{i,j} \in \mathbf{R}^{116\times116}$ that represent the relationship with 116 number of j ROIs. For example, in the p disease group, if the i ROI attention distribution has a high value with the j ROI, we can infer that the i ROI and j ROI have similar reaction patterns within the p disease group. Here, the sum of each row equals to one. Fig. 3 shows the attention distribution matrix of each pair of disease. In each attention distribution matrix, all values are consistently aligned by row indicating that there are certain ROIs that have consistent associations with other ROIs. Through this rationale, we are able to assume that the columns that contain ROIs with the brighter values sufficiently represent the unique characteristics of each disease. Fig. 3 shows that for the most part, the ROI's attention distribution network does not vary greatly (e.g., subtle differences in the color scheme) among the disease groups in question such as AD vs. MCI, AD vs. EMCI, AD vs. LMCI, and EMCI vs. LMCI. This phenomena occurs because the data from resting
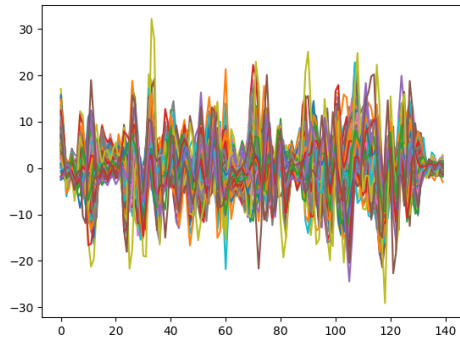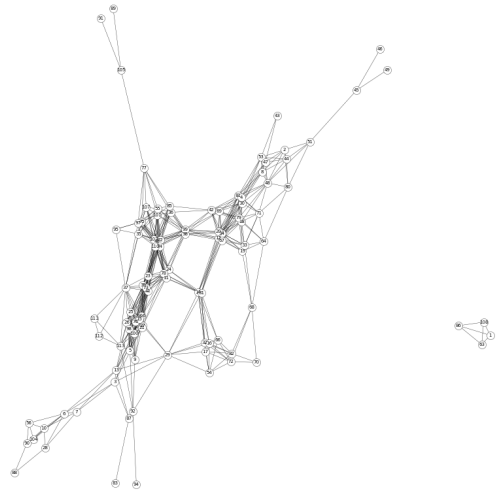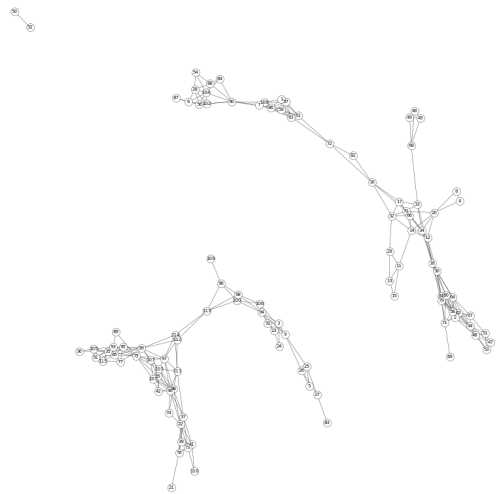
(a) rs–fMRI BOLD signal
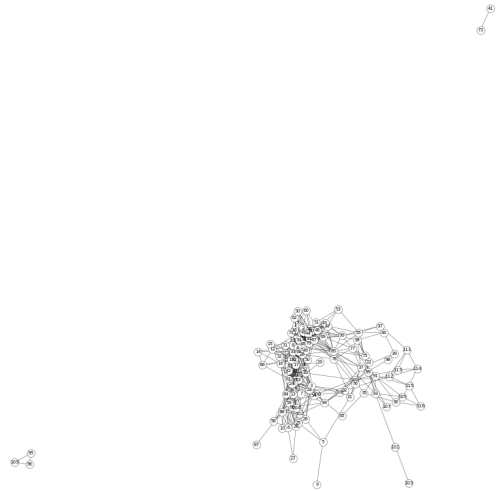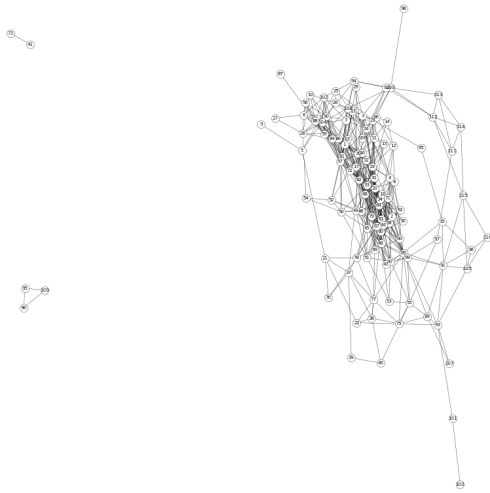
(b) Pearson's r–based FCN

(c) Fisher's z–based FCN

(d) Linear space–based FCN

(e) Stochastic space–based FCN

(f) Topological space–based FCN

Figure 2: Correlation coefficient–based FCN and latent space–based FCN

#	Name	#	Name	#	Name	#	Name
1	Precentral_L	30	Insula_R	59	Parietal_Sup_L	88	Temp_Pole_Mid_R
2	Precentral_R	31	Cingulum_Ant_L	60	Parietal_Sup_R	89	Temporal_Inf_L
3	Frontal_Sup_L	32	Cingulum_Ant_R	61	Parietal_Inf_L	90	Temporal_Inf_R
4	Frontal_Sup_R	33	Cingulum_Mid_L	62	Parietal_Inf_R	91	Cerebelm_Crus1_L
5	Frontal_Sup_Orb_L	34	Cingulum_Mid_R	63	SupraMarginal_L	92	Cerebelm_Crus1_R
6	Frontal_Sup_Orb_R	35	Cingulum_Post_L	64	SupraMarginal_R	93	Cerebelm_Crus2_L
7	Frontal_Mid_L	36	Cingulum_Post_R	65	Angular_L	94	Cerebelm_Crus2_R
8	Frontal_Mid_R	37	Hippocampus_L	66	Angular_R	95	Cerebelum_3_L
9	Frontal_Mid_Orb_L	38	Hippocampus_R	67	Precuneus_L	96	Cerebelum_3_R
10	Frontal_Mid_Orb_R	39	ParaHippo_L	68	Precuneus_R	97	Cerebelum_4_5_L
11	Frontal_Inf_Oper_L	40	ParaHippo_R	69	Paracentral_Lob_L	98	Cerebelum_4_5_R
12	Frontal_Inf_Oper_R	41	Amygdala_L	70	Paracentral_Lob_R	99	Cerebelum_6_L
13	Frontal_Inf_Tri_L	42	Amygdala_R	71	Caudate_L	100	Cerebelum_6_R
14	Frontal_Inf_Tri_R	43	Calcarine_L	72	Caudate_R	101	Cerebelum_7_L
15	Frontal_Inf_Orb_L	44	Calcarine_R	73	Putamen_L	102	Cerebelum_7_R
16	Frontal_Inf_Orb_R	45	Cuneus_L	74	Putamen_R	103	Cerebelum_8_L
17	Rolandic_Oper_L	46	Cuneus_R	75	Pallidum_L	104	Cerebelum_8_R
18	Rolandic_Oper_R	47	Lingual_L	76	Pallidum_R	105	Cerebelum_9_L
19	Supp_Motor_L	48	Lingual_R	77	Thalamus_L	106	Cerebelum_9_R
20	Supp_Motor_R	49	Occipital_Sup_L	78	Thalamus_R	107	Cerebelum_10_L
21	Olfactory_L	50	Occipical_Sup_R	79	Heschl_L	108	Cerebelum_10_R
22	Olfactory_R	51	Occipital_Mid_L	80	Heschl_R	109	Vermis_1_2
23	Frontal_Sup_Med_L	52	Occipical_Mid_R	81	Temporal_Sup_L	110	Vermis_3
24	Frontal_Sup_Med_R	53	Occipital_Inf_L	82	Temporal_Sup_R	111	Vermis_4_5
25	Frontal_Mid_Orb_L	54	Occipital_Inf_R	83	Templ_Pole_Sup_L	112	Vermis_6
26	Frontal_Mid_Orb_R	55	Fusiform_L	84	Templ_Pole_Sup_R	113	Vermis_7
27	Rectus_L	56	Fusiform_R	85	Temporal_Mid_L	114	Vermis_8
28	Rectus_R	57	Postcentral_L	86	Temporal_Mid_R	115	Vermis_9
29	Insula_L	58	Postcentral_R	87	Templ_Pole_Mid_L	116	Vermis_10

Table 2: Automated Anatomical Labeling–116 template

state was rarely affected by external factors. Nonetheless, the group classification performed yielded an average of 90% classification accuracy, demonstrating that the attention distribution network of each disease does indeed encompass subtle differences. Thus, we are able to infer that there are ROIs in each of the disease groups that can be grouped together in similar patterns.

Furthermore, based on the previously generated attention distribution, we extracted ROIs with large differences in distribution for each disease pair. Fig. 12 shows the regions with the greatest distribution differences for each disease group. We used the Kullback–Leibler Divergence (KLD) method to quantify the difference between the two distributions from each comparison pair. This was used in order to determine the distinctive ROIs with unique patterns that distinguishes the two groups. The greater KLD value of the ROI, the greater the attention distribution difference between the different disease groups. We appended the other diseases' groups of KLD values in the supplementary materials. Patients diagnosed with a high likelihood to develop AD showed significantly smaller Thalamus (77, 78) and Putamen (73, 74) volume, both which has been shown to have an effect on declining cognition in the AD population [24]. The top 3rd, 4th distinctive ROIs are Pallidum_R (76) and Pallidum_L (75). The 5th significant ROI is Hippocampus_R (38), for which both the volume and activation difference has been shown to be significant in the AD and MCI group [25, 26]. The 6th, 7th ROIs are Cerebelum_4_5_R (98), Cerebelum_4_5_L (97), which has generally been shown to be primarily related to sensorimotor control [27, 28]. Although the functional relevance of the Cerebellum in AD is still in its infancy, it has been suggested to be related to structural and functional cerebellar changes and the topography of neurodegeneration [29]. There has also been research suggesting that AD and frontotemporal dementia are related to the distinct and circumscribed atrophy in the Cerebellum [30].

We then compared AD with both EMCI and LMCI. First, when comparing AD and EMCI, the top 1 and 6 regions were Putamen_R (74), Putamen_L (73) respectively, top 2 was Hippocampus_R (38), and top 3 and 7 were Pallidum_R (76), Pallidum_L (75), respectively. Top–4,5 were Fusiform_R (56), Fusiform_L(55), and it is known the Fusiform (55, 56) is related to facial recognition [31]. Recent research has shown that EMCI patients show alteration in Fusiform

(55, 56) connectivity in the Middle occipital gyrus (52, 53) and Anterior cingulate (31, 32) [32]. When compared to AD and EMCI, the AD and LMCI disease pair group shows greater contrast differences in right Parahippocampal gyrus (40). The Parahippocampal gyrus (39, 40) is thought to be involved in the limbic system [33] as well as memory encoding and retrieval [34, 35, 36] showed that the Parahippocampal gyrus (39, 40) also plays a crucial role in the progression of LMCI to AD. Lastly, we compared early MCI and late MCI. The region with the greatest distribution differences between EMCI and LMCI was Fusiform_L (55), a region that previous research has shown to have functional connectivity differences between the two groups [37]. The region with the second most differences in distribution was right Middle frontal gyrus (8), which previous research has shown to exhibit a reduction in functional connectivity in LMCI compared to EMCI [38]. The top brain regions analyzed in the previous sections prove to be meaningful biomarkers and are supported by previous research.

Different patterns of ROIs from the attention–distribution

We then looked at regions that showed distribution differences for results based on the self–attention distribution classification model. In general, these ROIs were correlated based on location proximity and functional similarities rather than exhibiting individualized patterns. In order to decipher these types of dependent structures, this study utilized the attention distribution network generated from the classification model to generate a region network for each patient. By doing so, we were able to observe which regions showed characteristics of each disease despite individual differences. Furthermore, we could compare the characteristics of the different disease groups through ROI network connectivity.

We used the concept of LSIRM in this section to estimate the latent positions of nodes based on their connectivity. Because the original LSIRM models binary data, we adjusted the continuous version of LSIRM to model continuous values. In order to separate these strongly correlated ROIs, we extracted the top 25% of the attention distribution matrix columns with the highest probability and highest coefficient variation. Table 3 displays the top 29 unique ROIs that are highly correlated with a subset of brain regions. Using the network model, we aim to investigate how these top 29 unique ROIs are located as latent variables that represent the connection with other unique ROIs among the different disease pairs.

To process the network model, we constructed a matrix $\mathbf{M}_{n,r}, n = 1, \cdots, N_p, r = 1, \cdots, 29$ for each patient–ROIs. Here, N_p indicates the number of patients from each disease group $p = \{AD, MCI, EMCI, LMCI\}$. Based on this, we estimated the latent positions of these ROIs to identify the most commonly appeared as essential features in distinguishing the disease from the other diseases. We summarized the sub connectivity of ROIs and highlighted the ROI nodes in Section . Through this network connectivity, we are able to study which ROIs are meaningful in distinguishing between the different disease groups and also visualize the differences in functional clusters through studying the sub connectivity of these ROIs.

Step3: Summary of FCN Networks for each disease group using Network Model

Fig. 4 to 7 show the differences in disease network between the two groups. Blue indicates meaningful regions that show different values from the attention distribution matrix when compared to the other disease groups. The orange, on the other hand, indicates ROIs that were selected before analysis to be meaningful in both disease groups, but were shown to only be meaningful in one group post–analysis. Finally, green indicates regions that were meaningful in both disease groups. According to results from the continuous analysis LSIRM [15] used in the current study, we were able to decipher structural relationships of ROIs and extract ROIs that were significant in patients in all the disease groups. In order to see the overall connectivity, we explored connectivity structures in ROIs that were flagged to be significant in the disease network based on the FCN we established in Section . The higher saturation colors indicates high probability values that were assigned as meaningful features in all patient groups using LSIRM. Here, the ROI nodes which were not selected prior to LSIRM but are directly connected to the these ROIs were represented by the same color with a lower brightness level.
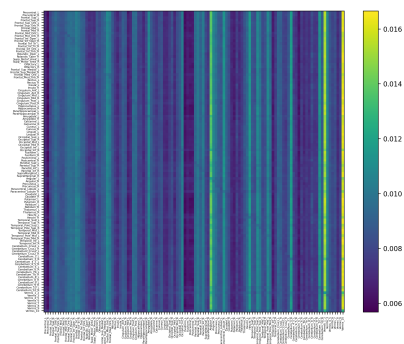
AD/MCI

According to Fig. 4 (a), Cluster A is comprised of Cerebelum_7_L (101) and Cerebelum_8_L (103). These two regions did not show activity in MCI, and the majority of regions that reacted in AD were connected to the Cerebellum regions. This difference can be seen the AD group shows smaller grey matter volume in the cerebellar anterior lobe compared to the non–AD group [39]. Cluster C with Hippocampus_R (38) and cluster D with Cingulum_Mid_L (33) and Cingulum_Mid_R (34) of Fig. 4 (a) show the cluster of regions and their direct connectivity that were more reactive in AD compared to MCI. Hippocampus_R (38) of cluster C showed greater reactivity in AD when compared to MCI
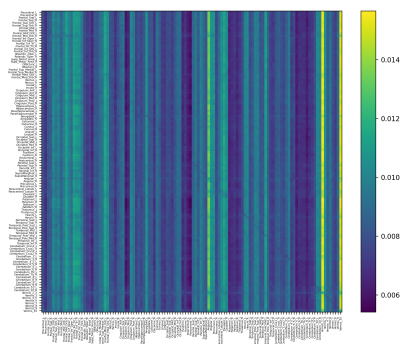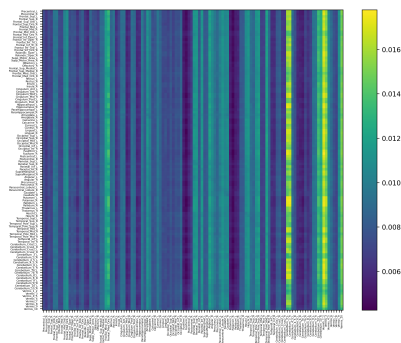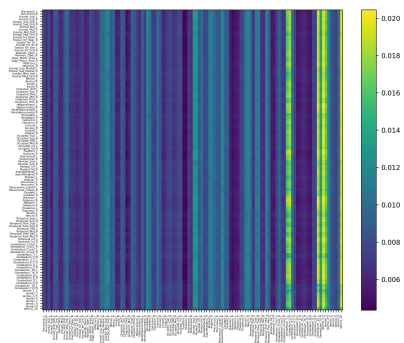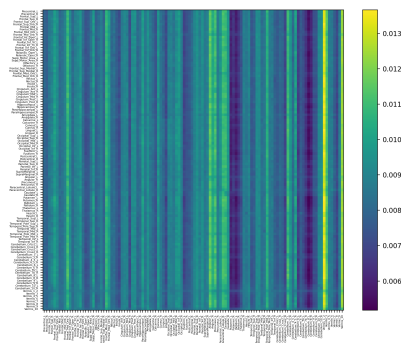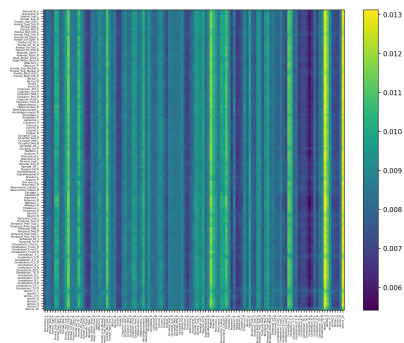
(a) AD (AD vs MCI)

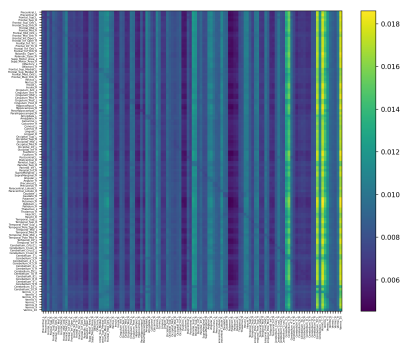(b) MCI (AD vs MCI)

(c) AD (AD vs EMCI)
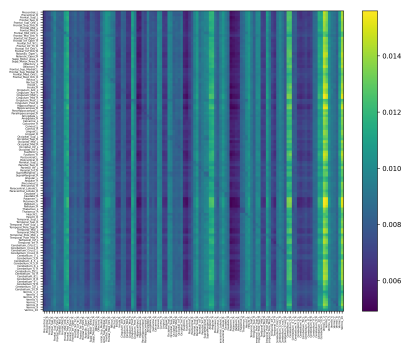
(d) EMCI (AD vs EMCI)

(e) AD (AD vs LMCI)

(f) LMCI (AD vs LMCI)

(g) EMCI (EMCI vs LMCI)

(h) LMCI (EMCI vs LMCI)

Figure 3: Attention distribution matrix of each pair of disease

Top	AD vs MCI		AD vs EMCI	
	AD	MCI	AD	EMCI
Top–1	Postcentral_L	Cingulum_Mid_L	Fusiform_R	Fusiform_L
Top–2	Postcentral_R	Postcentral_L	Cerebelum_6_L	Temporal_Inf_L
Top–3	Temporal_Inf_L	Fusiform_R	Pallidum_R	Cingulum_Mid_L
Top–4	Supp_Motor_Area_R	Precentral_R	Postcentral_L	Pallidum_R
Top–5	Fusiform_L	Pallidum_L	Fusiform_L	Fusiform_R
Top–6	Cingulum_Mid_L	Temporal_Inf_L	Cerebelum_6_R	Frontal_Inf_Orb_L
Top–7	Fusiform_R	Fusiform_L	Hippocampus_R	Cerebelum_6_L
Top–8	Cerebelum_8_R	Supp_Motor_Area_R	Cingulum_Mid_L	Frontal_Inf_Tri_R
Top–9	Cerebelum_6_L	Insula_L	Cerebelum_7b_L	Putamen_R
Top–10	Putamen_L	Cerebelum_6_R	Putamen_R	Cingulum_Mid_R
Top–11	Cerebelum_8_L	Cerebelum_4_5_R	Cerebelum_4_5_L	Cerebelum_6_R
Top–12	Precentral_R	Postcentral_R	Temporal_Inf_L	Temporal_Inf_R
Top–13	Thalamus_L	Cerebelum_4_5_L	Cingulum_Mid_R	Vermis_8
Top–14	Temporal_Mid_R	Cerebelum_6_L	Cerebelum_8_L	Insula_L
Top–15	Cerebelum_4_5_R	Putamen_R	Hippocampus_L	Pallidum_L
Top–16	Insula_R	Cerebelum_8_R	Rolandic_Oper_R	Frontal_Sup_R
Top–17	Rolandic_Oper_R	Cerebelum_Crus2_R	Pallidum_L	Cerebelum_9_R
Top–18	Precentral_L	SupraMarginal_R	Cerebelum_Crus2_L	Temporal_Sup_R
Top–19	Temporal_Inf_R	Rolandic_Oper_R	Cerebelum_7b_R	Postcentral_L
Top–20	Insula_L	Hippocampus_R	Putamen_L	Cerebelum_7b_L
Top–21	Putamen_R	Cingulum_Mid_R	Temporal_Inf_R	Cerebelum_8_R
Top–22	Cerebelum_7b_R	Pallidum_R	Insula_L	Rolandic_Oper_L
Top–23	Temporal_Mid_L	Thalamus_L	Cerebelum_Crus2_R	Putamen_L
Top–24	Hippocampus_R	Putamen_L	Rolandic_Oper_L	Rolandic_Oper_R
Top–25	Cerebelum_4_5_L	Vermis_4_5	Cerebelum_8_R	Insula_R
Top–26	Cerebelum_10_R	Paracentral_Lobule_L	Cerebelum_3_L	Cerebelum_Crus2_L
Top–27	Cingulum_Mid_R	Vermis_8	Frontal_Inf_Tri_R	Cerebelum_3_L
Top–28	Pallidum_L	Precentral_L	Frontal_Sup_R	Frontal_Inf_Tri_L
Top–29	Cerebelum_7b_L	Supp_Motor_Area_L	Lingual_R	Hippocampus_R

Top	AD vs LMCI		EMCI vs LMCI	
	AD	LMCI	EMCI	EMCI
Top–1	Pallidum_L	Cerebelum_8_L	Putamen_L	Putamen_L
Top–2	Putamen_L	Cerebelum_8_R	Putamen_R	Fusiform_R
Top–3	Cerebelum_8_L	Pallidum_R	Pallidum_R	Pallidum_L
Top–4	Cerebelum_8_R	Putamen_L	Pallidum_L	Putamen_R
Top–5	Putamen_R	Pallidum_L	Temporal_Inf_L	Hippocampus_R
Top–6	Pallidum_R	Putamen_R	Fusiform_L	Pallidum_R
Top–7	Cerebelum_6_L	Hippocampus_R	Fusiform_R	Fusiform_L
Top–8	Cerebelum_7b_R	Vermis_8	Temporal_Inf_R	Hippocampus_L
Top–9	Fusiform_L	Cerebelum_7b_L	Hippocampus_R	Temporal_Inf_R
Top–10	Insula_R	Cerebelum_6_L	Insula_L	Temporal_Inf_L
Top–11	Cerebelum_Crus2_R	Cerebelum_4_5_R	Olfactory_R	Cingulum_Mid_R
Top–12	Vermis_8	Fusiform_R	Rolandic_Oper_R	Thalamus_L
Top–13	Vermis_7	Cingulum_Mid_R	Cerebelum_6_L	Cerebelum_6_L
Top–14	Cerebelum_9_R	Vermis_6	Temporal_Mid_R	Insula_R
Top–15	Lingual_R	Cerebelum_9_R	Insula_R	Cerebelum_4_5_L
Top–16	Cerebelum_6_R	Thalamus_L	Frontal_Inf_Orb_R	Cerebelum_8_L
Top–17	Hippocampus_R	Cerebelum_7b_R	Hippocampus_L	Olfactory_R
Top–18	Fusiform_R	Temporal_Mid_R	Rolandic_Oper_L	Insula_L
Top–19	Cerebelum_4_5_R	Cerebelum_6_R	Cerebelum_7b_R	Cingulum_Mid_L
Top–20	Cerebelum_9_L	Cerebelum_4_5_L	Cerebelum_7b_L	Cerebelum_6_R
Top–21	Cerebelum_7b_L	Vermis_7	Cingulum_Mid_R	Rolandic_Oper_R
Top–22	Insula_L	Cerebelum_Crus2_R	ParaHippo_R	Precentral_L
Top–23	Olfactory_L	Insula_L	Cerebelum_3_R	ParaHippo_R
Top–24	Rolandic_Oper_L	Olfactory_R	Thalamus_R	Cerebelum_4_5_R
Top–25	Olfactory_R	Rectus_L	Thalamus_L	Cerebelum_7b_R
Top–26	Precuneus_L	Temporal_Inf_R	Olfactory_L	Thalamus_R
Top–27	Cerebelum_Crus1_L	Temporal_Mid_L	Cingulum_Mid_L	ParaHippo_L
Top–28	Rolandic_Oper_R	Rolandic_Oper_L	Frontal_Med_Orb_R	Temporal_Mid_R
Top–29	Thalamus_L	Lingual_R	Cerebelum_4_5_R	Amygdala_L

Table 3: This table displays the top 29 ROIs that show distribution differences between disease group pairs.

and Hippocampus (37, 38), ParaHippo (39, 40), Putamen (73, 74), Pallidum (75, 76), Amygdala (41, 42) are densely populated in this area.

Cluster F of Fig. 4 (b) shows ROIs, Postcentral_L (57) and Postcentral_R (58), that were more reactive in MCI compared to AD. This Postcentral (57, 58) is directly connected to Cingulum_Mid (33, 34), Precentral (1, 2), Paracentral_Lob_L (69).

Cluster B of Fig. 4 (a) and Cluster E of Fig. 4 (b) corresponds to Cerebelum 4_5_R (98) that reacted to both AD and MCI. Both results show that Cerebelum 4_5_R (98) is not only connected with other Cerebellum regions, but is also directly connected to Fusiform_L (55) and Fusiform_R (56), regions that are related to facial recognition.

AD/EMCI

Cluster A and B of Fig. 5 (a), which are Hippocampus_L (37), Lingual_R (48), Cerebelum_4_5_L (97), were found to be meaningful regions not in EMCI but only in AD. Hippocampus (37, 38) in both hemispheres are directly connected. These regions are also directly connected to ParaHippo (39, 40), Putamen (73, 74), Pallidum (75, 76), Amygdala (41, 42) and the results are similar to the results described in Section . Fusiform_R (56)and Cerebelum_8_L (103) are directly connected to Hippocampus_R (38), and are similar to cluster A and B of Fig. 4 (a). Hippocampus_L (37) and Lingual_R (48) are not only directly connected to Lingual_L (47), but also to Calcarine (43, 44), Cuneus (45, 46), Fusiform_L (56) and Cerebelum_6_L (99). Cluster D and E of Fig. 5 (a) were more active in AD relative to EMCI and included the Hippocampus_R (38), Rolandic_Oper_R (18) regions. We are able to see that Rolandic_Oper_R (18) is directly connected to Putamen (73, 74), Pallidum (75, 76) and Heschl_L (79).

Cluster F of Fig. 5 (b) was active in EMCI but not AD, and Cerebelum_9_R (106) was analyzed. This region was adjacent to Cerebelum_Crus2_R (94), Cerebelum_7b_R (102) and Cerebelum_9_L (105). Cluster H, I and J of Fig. 5 (b) are regions that were more active in EMCI relative to AD, and regions Cingulum_Mid_L (33), Cingulum_Mid_R (34), Pallidum_L (75) and Cerebelum_Crus2_L (93) were analyzed. Cingulum_Mid is directly connected to Precentral (1, 2), Supp_Motor (19, 20), Postcentral (57, 58) and SupraMarginal (63, 64).

Cluster C of Fig. 5 (a) and cluster G of (b) are regions that were active in both AD and EMCI, and corresponds to Fusiform_L (55) and Fusiform_R (56). Fusiform (55, 56) is directly connected with Hippocampus (37, 38) and ParaHippo (39, 40).

AD/LMCI

Cluster A of Fig. 6 (a) was active in AD but not LMCI, and Temporal_Mid_R(86) was analyzed. Cluster B of Fig. 6 (a) reacted more in AD relative to LMCI, and Cerebelum_6_L (99) was analyzed. Not only is this region connected with multiple Cerebelum (91, 92, 100) areas, but is also connected to Fusiform_L (55), Lingual (47, 48), multiple Vermis (112, 113, 114).

Cluster C of Fig. 6 (b) was active only in LMCI and not AD, and Rolandic_Oper_R (18) was analyzed. This region was connected with Heschl (79, 80), Insula (29, 30) and Temporal_Sup (81, 82). Cluster D, E, and F of Fig. 6 (b) are regions more active in LMCI relative to AD, and regions Putamen_L (73), Cerebelum_4_5_R (98) and Vermis_8 (114) were analyzed. Putamen (73, 74) is connected to Olfactory (21, 22), Hippocampus (37, 38), Amygdala (41, 42), Pallidum (75, 76) and Thalamus_L (77).

EMCI/LMCI

Cluster A, B, and C of Fig. 7 (a) were regions that were only active in EMCI, and Frontal_Inf_Orb_R (16), Frontal_Med_Orb_R (26), and Cerebelum_3_R (96) were analyzed. Cerebelum_3_R (96) is directly connected to Cerebelum_3_L (95) and Vermis_3 (110). ROIs that are connected to Frontal_Inf_Orb (15, 16) and Frontal_Inf_Tri (13, 14), can be grouped as Frontal regions. We can also see that they are directly connected to Putamen_R (74). The Frontal_Med_Orb_R (26) is directly connected to Frontal_Med_Orb_L (25), Rectus (27, 28), and Frontal_Sup_Orb_R (6). Cluster D are regions that were more active in EMCI relative to LMCI, and include Putamen_L (73), Pallidum_L (75) regions. The ROIs that were primarily connected to these regions can largely be defined as Caudate (71, 72), Pallidum_R (76), Thalamus (77, 78), Hippocampus (37, 38), and Insula (29, 30). Other regions include Rolandic_Oper_L (17), Amygdala_R (42), Fusiform_L (55), and Cerebelum_8_L (103).

Fig. 7 (b), on the other hand, shows the FCN extracted for LMCI, which shows no significant ROIs that were significantly active only in LMCI. There is, however, cluster E, that shows ROIs more active in LMCI relative to EMCI. This cluster is comprised of ROIs connected to Temporal_Mid_R(86) and Cerebelum_6_L (99). Temporal_Mid_L (85) and Temporal_lnf_R(90) are ROIs connected with Temporal_Mid_R (86). ROIs connected with Cerebelum_6_L (99) are

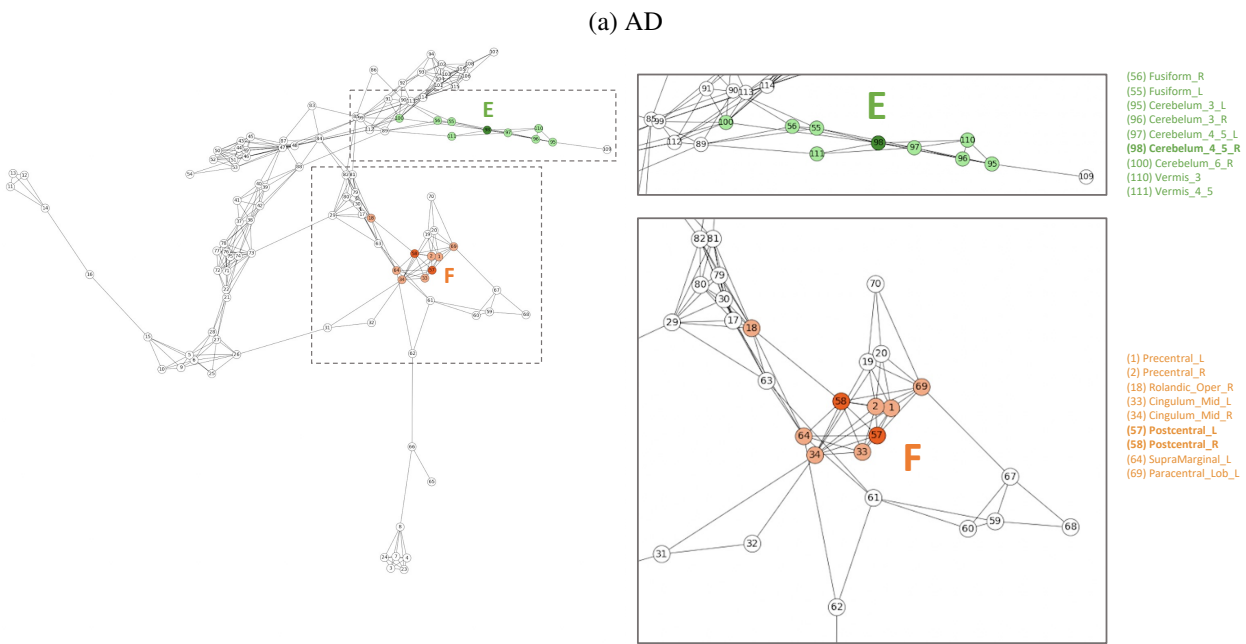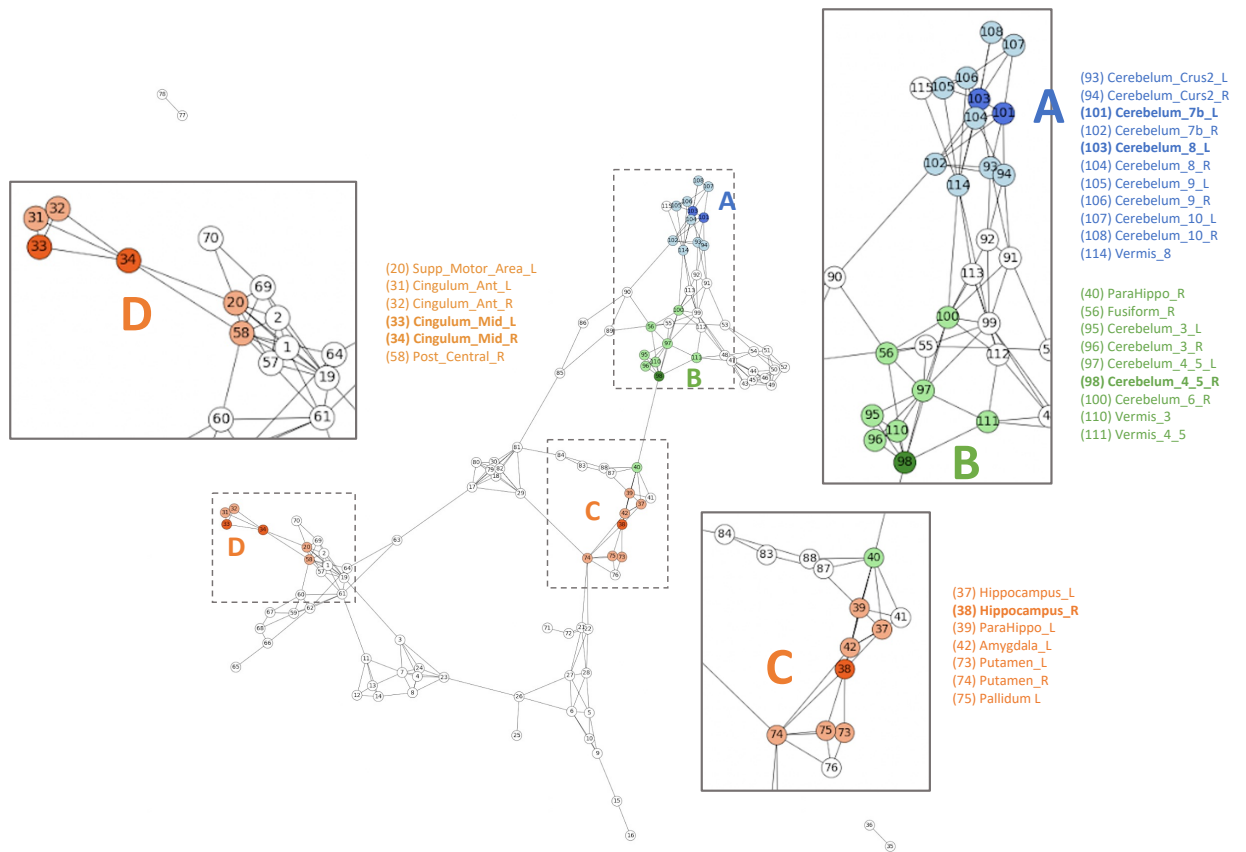(93) Cerebelum_Crus2_L
(94) Cerebelum_Curs2_R
(101) Cerebelum_7b_L
(102) Cerebelum_7b_R
(103) Cerebelum_8_L
(104) Cerebelum_8_R
(105) Cerebelum_9_L
(106) Cerebelum_9_R
(107) Cerebelum_10_L
(108) Cerebelum_10_R
(114) Vermis_8

(40) ParaHippo_R
(56) Fusiform_R
(95) Cerebelum_3_L
(96) Cerebelum_3_R
(97) Cerebelum_4_5_L
(98) Cerebelum_4_5_R
(100) Cerebelum_6_R
(110) Vermis_3
(111) Vermis_4_5

(20) Supp_Motor_Area_L
(31) Cingulum_Ant_L
(32) Cingulum_Ant_R
(33) Cingulum_Mid_L
(34) Cingulum_Mid_R
(58) Post_Central_R

(37) Hippocampus_L
(38) Hippocampus_R
(39) ParaHippo_L
(42) Amygdala_L
(73) Putamen_L
(74) Putamen_R
(75) Pallidum L

(a) AD

(56) Fusiform_R
(55) Fusiform_L
(95) Cerebelum_3_L
(96) Cerebelum_3_R
(97) Cerebelum_4_5_L
(98) Cerebelum_4_5_R
(100) Cerebelum_6_R
(110) Vermis_3
(111) Vermis_4_5

(1) Precentral_L
(2) Precentral_R
(18) Rolandic_Oper_R
(33) Cingulum_Mid_L
(34) Cingulum_Mid_R
(57) Postcentral_L
(58) Postcentral_R
(64) SupraMarginal_L
(69) Paracentral_Lob_L

(b) MCI

Figure 4: Network Summary in AD vs MCI

12

(a) AD

(b) EMCI
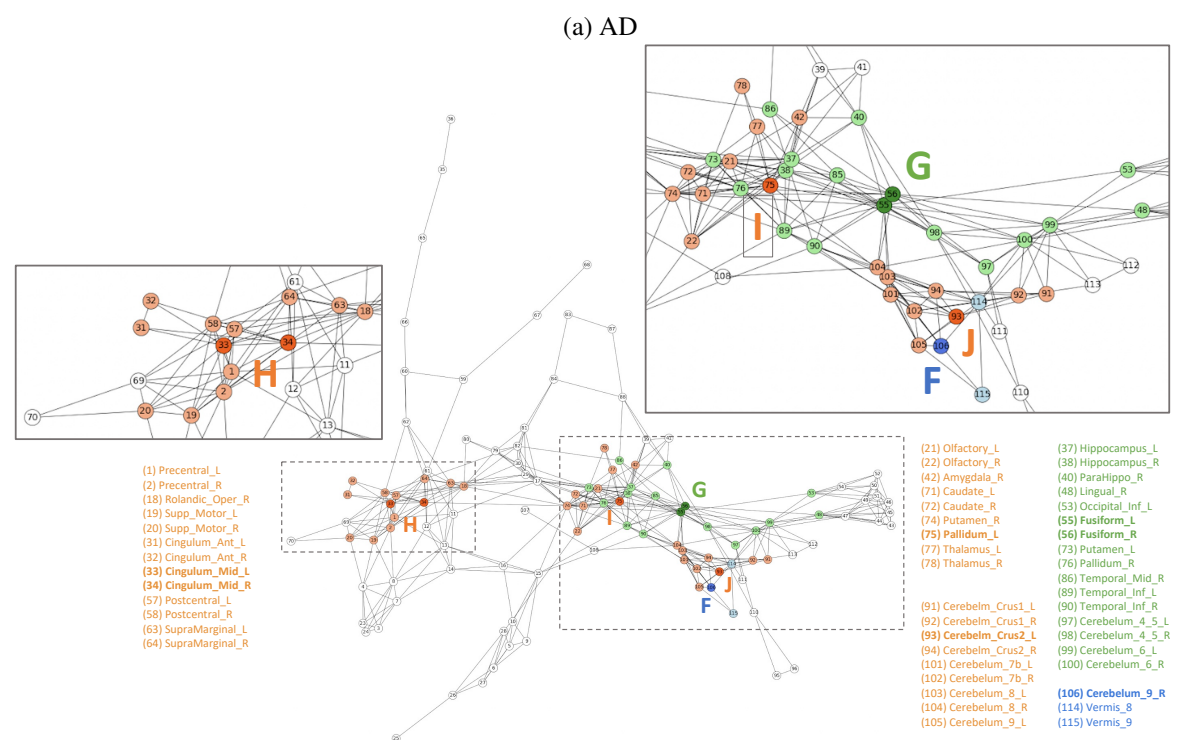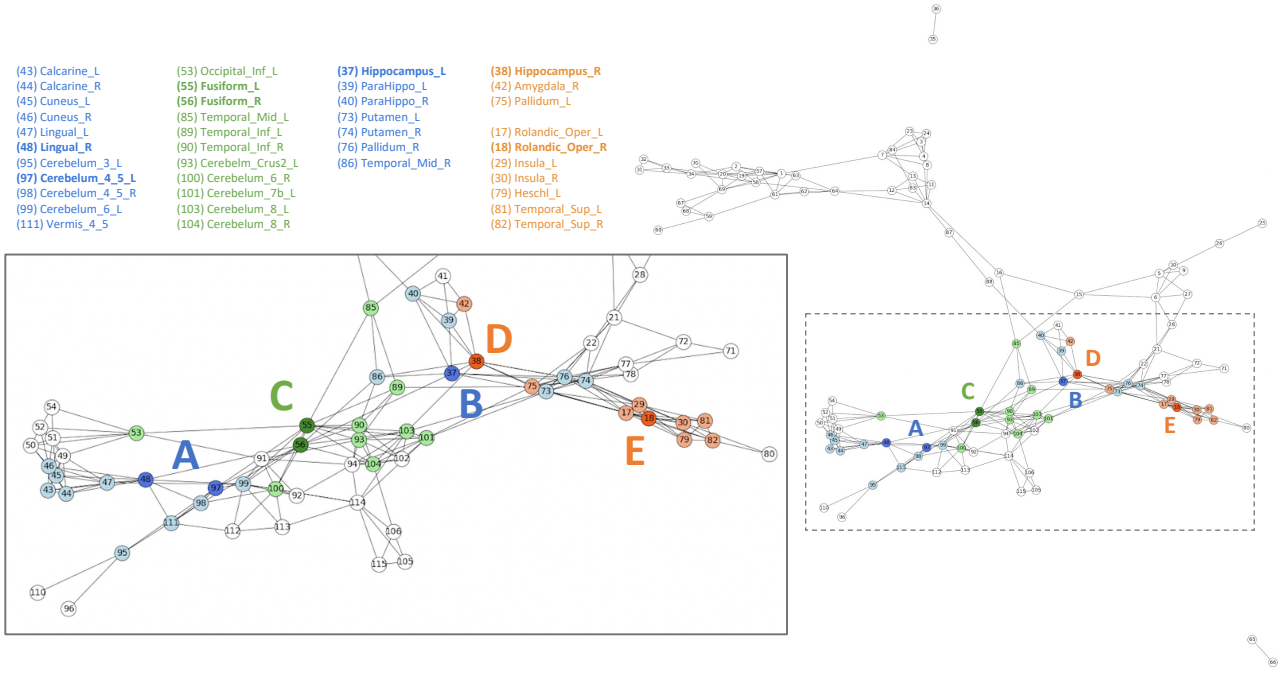
Figure 5: Network Summary in AD vs EMCI

(a) AD

(85) Termporal_Mid_L
(86) Termporal_Mid_R
(90) Termporal_Inf_R

(47) Lingual_L
(48) Lingual_R
(55) Fusiform_L
(91) Cerebelm_Crus1_L
(92) Cerebelm_Crus1_R
(97) Cerebelum_4_5_L
(99) Cerebelum_6_L
(100) Cerebelum_6_R
(112) Vermis_6
(113) Vermis_7
(114) Vermis_8

(b) LMCI

(17) Rolandic_Oper_L
(18) Rolandic_Oper_R
(29) Insula_L
(30) Insula_R
(79) Heschl_L
(81) Temporal_Sup_L
(82) Temporal_Sup_R

(21) Olfactory_L
(22) Olfactory_R
(37) Hippocampus_L
(38) Hippocampus_R
(40) ParaHippo_R
(41) Amygdala_L
(42) Amygdala_R
(73) Putamen_L
(74) Putamen_R
(75) Pallidum_L
(76) Pallidum_R
(77) Thalamus_L

(56) Fusiform_R
(96) Cerebelum_3_R
(97) Cerebelum_4_5_L
(98) Cerebelum_4_5_R
(100) Cerebelum_6_R
(101) Cerebelum_7b_L
(105) Cerebelum_9_L
(106) Cerebelum_9_R
(110) Vermis_3
(113) Vermis_7
(114) Vermis_8

Figure 6: Network Summary in AD vs LMCI

14

largely Fusiform (55, 56), Lingual (47, 48), and multiple Vermis (112, 113). Other regions include Cerebelum_Crus1_L (91), Cerebelum_4_5_L (97), and Cerebelum_6_R (100).

Discussion

In this paper, we provide a unique analytical methodology for determining the network structure of different disease groups. To summarize, we first built the FCN, which depicted the associated connections between the ROIs. It aids in the summarization of overall structure by projecting complicated data into a low–dimensional structure in order to demonstrate the relationships between ROI functions. We built the FCN on the basis of these relationships. By employing each patient's FCN, we estimated the ROI distribution using the classification model of the self–attention deep learning. By taking into account the correlated complex structure, our method takes advantage of capturing the ROIs signal patterns without losing information. Through our new model, classification accuracy between two different disease groups can be increased greatly. Therefore, the output of ROIs distributions is validated to reveal the hidden traits that distinguishes between the different disease groups.

Despite the fact that the self–attention model validates FCN from each patient and outputs the ROIs attention distribution of each patient, we still need to determine the overall significant ROIs among patients who represent each cognitive disease group. To extract meaningful ROIs from the ROIs distribution, we used the latent space item response network model that can extract the important ROIs by considering the interactions among ROIs from each patient. Section shows the result of meaningful clusters based on the ROIs extracted from the network model. These clusters denote connection subgroups, each of which is formed of the network model's most important ROI functions and their first direct connections in FCN. This enables a more in–depth understanding of the peculiarities of different illnesses by evaluating ROIs dependence structure.

Our method also revealed significant biological findings, which have been steadily verified through several studies. Therefore, these convincing findings validates our method to determining the features of cognitive diseases in a more intuitive manner by examining ROI connectivity. Here, not only did our research provide comparable results to prior extensive works, but it also identified that the Cerebellum is a growing function that has lately been researched for cognitive impairment.
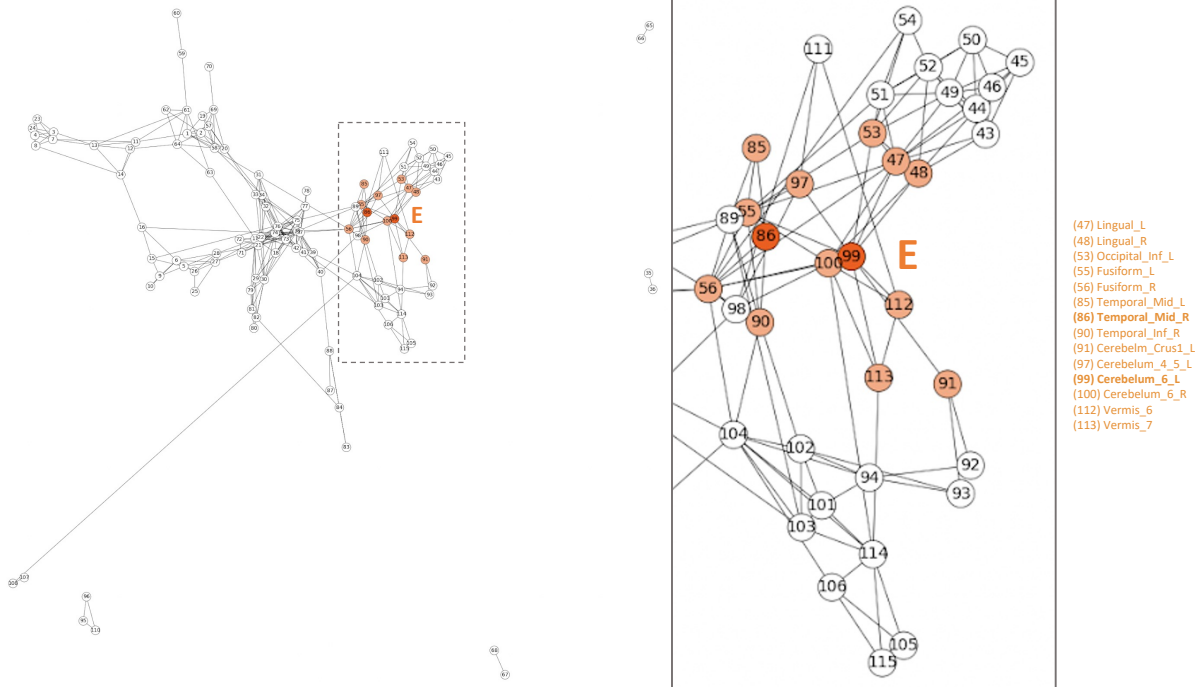
First, when comparing AD to MCI, we discovered that the Hippocampus (37, 38) plays an important role in expressing AD characteristics (Fig. 4(a) Cluster C). Many studies have shown that having Hippocampus (37, 38) dysfunction affects memory [40, 41, 42]. Based on our approach, We also discovered connections between Hippocampus (37, 38) and Putamen (73, 74) and ParaHippo (39, 40), which have been linked to cognitive impairment in Alzheimer's disease [43, 44, 24]. When compared to EMCI, the biomarkers in AD may be clearly revealed (Fig. 5 (a)). These biomarkers are detected in connections between Hippocampus (37, 38) and ParaHippo (39, 40), Putamen (73, 74), Pallidum (75, 76), and Amgydala (41, 42) [45, 46, 47].

Second, our method provides additional information about Cingulum_Mid (33, 34) towards MCI, which is solely regarded as one of the most important ROI in AD [48, 49, 50, 51, 52]. Cingulum_Mid (33, 34) is responsible for processing motor and attention–related activities [53]. However, our method discovered that Cingulum_Mid (33, 34) is more prominent in MCI and EMCI than in AD (Fig. 4 (a), Fig. 4 (b), Fig. 5 (b)). According to our findings, Cingulum_Mid (33, 34) is linked to the Postcentral (57, 58), Precentral (1, 2), and Paracentral_Lob (69, 70), all of which are known to process motor information. The fluorodeoxyglucose(FDG) positron emission tomography(PET) modality has been used to investigate all four of the above–mentioned areas as relevant indicators in MCI [54]. Furthermore, the overall fractional anisotropy value of Cingulum_Mid (33, 34) in MCI differs from that of other cognitive illness groups [53]. In the network of EMCI compared to AD, our model found that Cingulum_Mid (33, 34) is linked to Supramarginal (63, 64), which is associated to motor attention–related activity (Fig. 5 (b)). These linkages have lately been examined in relation to planning and cognitive control processing [55, 56]. As a result, Cingulum_Mid (33, 34), which has previously gone unnoticed, should be regarded a cognitive as well as a motor function in MCI and EMCI.

Third, Fusiform (55, 56) is the ROI that is important in revealing the characteristics of both AD and MCI. Fusiform (55, 56) is known for processing facial recognition [31]. Recently, Fusiform (55, 56) has been studied for revealing the genetic and epigenetic basis of AD [57]. Our method showed that Fusiform (55, 56) is both widely reacted as significant ROI of AD and EMCI (Fig. 5 (a), (b)) and Fusiform (55, 56) is connected to Cerebellum functions. This connection shows consistency in all network results (Fig. 4– 6). According to the global hub node centrality analysis [58], Fusiform (55, 56) and Cerebellum regions play important roles in constituting the key makeup of disease characteristics of MCI. As such, we are able to observe through our model that Fusiform (55, 56) and Cerebellum regions, which play key roles in both MCI and AD, are greatly related to one another.

(17) Rolandic_Oper_L
(21) Olfactory_L
(22) Olfactory_R
(29) Insula_L
(30) Insula_R
(37) Hippocampus_L
(38) Hippocampus_R
(42) Amygdala_L
(55) Fusiform_L
(71) Caudate_L
(72) Caudate_R
(73) Putamen_L
(75) Pallidum_L
(76) Pallidum_R
(77) Thalamus_L
(78) Thalamus_R
(89) Temporal_Inf_L
(103) Cerebelum_8_L

(95) Cerebelum_3_L
(96) Cerebelum_3_R
(110) Vermis_3

(6) Frontal_Sup_Orb_R
(10) Frontal_Mid_Orb_R
(13) Frontal_Inf_Tri_L
(14) Frontal_Inf_Tri_R
(15) Frontal_Inf_Orb_L
(16) Frontal_Inf_Orb_R
(25) Frontal_Mid_Orb_L
(26) Frontal_Mid_Orb_R
(27) Rectus_L
(28) Rectus_R
(74) Putamen_R

(a) EMCI

(47) Lingual_L
(48) Lingual_R
(53) Occipital_Inf_L
(55) Fusiform_L
(56) Fusiform_R
(85) Temporal_Mid_L
(86) Temporal_Mid_R
(90) Temporal_Inf_R
(91) Cerebelm_Crus1_L
(97) Cerebelum_4_5_L
(99) Cerebelum_6_L
(100) Cerebelum_6_R
(112) Vermis_6
(113) Vermis_7

(b) LMCI

Figure 7: Network Summary in EMCI vs LMCI

16

Last but not least, our methodology determined that the Cerebellum is a significant ROI function in investigating AD. Originally, the Cerebellum was thought to have a required function for exercise and activity [59, 60]. There have been several research that the Cerebellum is related to processing cognitive function [61, 62, 63] and emotional modulation [64]. Recently, the Cerebellum has been assigned as useful biomarkers in clinical AD patients [65]. According to our result, Cerebelum_4_5_R (98) has a significant ROI function in both AD and MCI(Fig. 4 (a), (b)). This finding is consistent with a research that investigated at spatial patterns of brain activity and found that both AD and MCI had decreased activity in Cerebelum_4_5_R (98) compared to the control group [66]. However, in terms of Cerebellum_8_L (103), we discovered that this ROI function exhibited higher response in AD compared to MCI(Fig. 4 (a)), resulting in the same finding in global brain connectivity (GBC) research [67]. The preceding results suggest that Cerebellum should be considered in both AD and MCI.

Methods

fMRI Data

In this study, we utilized resting-state fMRI (rs–fMRI) data collected from Alzheimer disease (AD), early mild cognitive impairment (EMCI), mild cognitive impairment (MCI), late mild cognitive impairment (LMCI), and control groups from Alzheimer's disease neuroimaging initiative (ADNI) dataset. The ADNI dataset is composed of four consecutive cohorts (ADNI1, ADNI2, ADNI–GO, and ADNI3). Participants were recruited for initial periods in the ADNI1 cohorts (October 2004). Follow–up of participants were recruited to the ADNI3 cohort period. To facilitate preprocessing of the fMRI data, we filtered data with the same acquisition protocols as the database. A total of three protocol conditions (200 timepoints, TR = 3000 ms, 48 slices) were applied for selection. After filtering based on three conditions, a total of 552 participants remained in the ADNI2, ADNI-go, and ADNI3 cohorts. The ADNI1 cohort was excluded because it did not contain data that met the aforementioned conditions. As a result, we used axial rs-fMRI data from 57 AD patients, 93 EMCI patients, 53 LMCI patients, 78 MCI patients, and 272 control participants.

MRI Acquisition

The participants included in this study participated in scanning at diverse sites through 3T MRI scanners manufactured by Philips Medical Systems or Siemens Healthineers. The detailed MRI protocols of the ADNI dataset were reported in the webpage (http://adni.loni.usc.edu/methods/mri-tool/mri-acquisition/). In the ADNI2 and ADNI-go cohorts, MRI scanning was performed at twenty-six different sites with Philips 3T MRI scanners, using synchronized scanning parameters. In the case of the ADNI3 cohort, Siemens 3T MRI scanners were used to collect fMRI data with synchronized parameters.

MRI Preprocessing

All scanned imaging data included in the ADNI database was checked for their quality by trained analysts. Two levels of quality control were performed. First, consistency of protocol parameters was investigated. Second, series-specific quality such as body motion, anatomic coverage, and other artifacts were checked. After conducting two levels of quality control, each image was classified as four quality labels (1 to 3: acceptable and 4: unusable). We preprocessed rs–fMRI data whose quality was acceptable for our research. To extract region of interest (ROI) time courses from rs–fMRI data, SPM12 (www.fil.ion.ucl.ac.uk/spm/) and DPARSFA toolbox (V5.1, http://rfmri.org/dpabi) was applied. The default preprocessing pipeline for ROI time courses extraction was used, including slice-time correction, realignment, normalization with Echo Planar Imaging(EPI) template, detrending, and smoothing with 6mm kernel. Temporal filtering with a range from 0.01Hz to 0.1Hz was performed to remove physiological noises. After preprocessing, we obtained temporal signals, correlation coefficient, and Fisher's Z–transformed correlation coefficients.

Dimension Reduction

To define functional connectivity, we first need to map ROIs latent locations into R2 space using dimension reduction. Since we were interested in the connectivity of ROIs from each patient, we reduced signal data of ROIs into ROIs with two coordinates by training their signal pattern similarity among ROIs. We began by embedding the ROIs time series data on R2 space using three dimension reduction methods: (1) Principal Component Analysis (PCA), t–Stochastic Neighbor Embedding (t–SNE), and Uniform Manifold Approximation and Projection (UMAP). However, since dimension methods only return the latent position of ROIs, it is crucial to define connections between ROIs using their latent position on R2 space. To accomplish this, we used TDA's mapper [9] to implement partial clustering, which we then used to define connections. If some ROIs are assigned to the same cluster, those ROIs are assumed to be

connected to one another. Similarly, we can apply this concept to other partial clusters that define connections from local to global connections at the end. As a result, we could construct the FCN of each patient.

Principal component analysis (PCA)

PCA is a technique that uses orthogonal transformation to reduce high-dimensional data to low-dimensional data. It converts high-dimensional space samples that are likely to be related to each other into low-dimensional space samples (main components) that are not linearly related. The axis with the most significant variance is the first principal component, and the second greatest variance is the second principal component. This decomposition divides the sample into the components that best represent the differences of information that have important implications for data analysis.

t-Stochastic Neighbor Embedding (t–SNE)

t–SNE is a non-linear dimension reduction method that aids in understanding the data with impact information. It is based on t-distribution, which is comparable to normal distribution but has the heavy–tail component that is helpful in covering up the far distribution element of high dimensional data. When two data construct similar structures, they nearly correspond to each other based on the similarity value from the t-distribution. The t–SNE results depict the embedded points whose distances, trained by calculating the points' resemblance in structure. reflect their degree of similarity.

Uniform Manifold Approximation and Projection (UMAP)

UMAP is a nonlinear dimension reduction method that models the manifold using a topological structure. Because it is based on topological space, the embedding points are close in proximity if the two data points have similar topological features. It first reorganizes the data into a fuzzy simplicial complex, which then produces the connections based on the hyper-parameter that controls the connectivity around the data. Then, it projects the connected data into a low-dimensional space based on their connection, where the connection indicates the aforementioned close proximity.

Mapper

The mapper can achieve the complexity of the topological space by combining and calculating simple values such as points, lines, triangles, etc. There are two main steps for this process. First, high-dimensional topological space data is transferred into a measure space such as a real space represented as a graph. This function could be any real function that reflects the characteristics of the data. In the next step, the graph is split into countable subsets of data, and is then clustered within subsets. This process is implemented to explore the interrelationships between the subsets, which will identify the structural relationships within the data. Each cluster becomes a node, and each node is connected to other nodes when they share the same data attributes. The network generated based on these nodes and connections enables the topological structure of high-dimensional data to be expressed in a $k-$simplex.

Partial Clustering

Partial clustering employs any standard clustering algorithm towards subsets of the original data set and then analyzes the interactions between the sub–clusters formed in this manner. If U and V are non–empty subsets of the data set, then the sub–clusters formed by each U and V may have non-empty intersections, which are used to construct a simplicial complex. These sub-clusters are referred to as vertices or nodes, and the non–empty intersection between clusters is referred to as an edge. This process results in a simple complex of dots, lines, and triangles that can be used to infer the topological structure of high-dimensional data.

Self–Attention Deep Model (Self–Attn)

Attention Mechanism is used to focus on specific input values from sequence-based tasks that is most relevant to the input in order to reduce information loss and increase information power [13]. Basically, our self–attention mechanism takes into account the temporal context of the spatially embedded representations and assigns relatively higher weights to time points at which the corresponding representations carry informative features for a target task. Here, the informativeness is determined adaptively with the learnable parameters in combination with other objectives.

The inputs here are the encoding values of the adjacency matrix among ROIs calculated from the FCN generated in this study. Thus, each input has query, key, value vector values. If we assume there are a total R number of ROIs, we can express that $Q_r \in \mathbf{R}^d, K_r \in \mathbf{R}^d$ and $V_r \in \mathbf{R}^d$ where $r = 1, \cdots, R$. Based on these features, the output of the

attention layer output is as follows:

$$Y_{\text{ROI}_r} = \sum_{j=1}^{R} (\text{Softmax}(Q_r K_j^\top) V_j), \tag{1}$$

where $r, j = 1, \cdots, R$. Therefore, the final Y_{ROI_r} is not simply a vector with ROI_r information but a ROI_r vector that reflects information about ROI connectivity. If we collect these vectors and compute them as a matrix, we are able to generate a self–attention matrix about ROIs. By multiprocessing Self–attention like those mentioned above, we utilized multi–head self–attention that jointly learns information about different location interactions. This study applied a total of 128 parallel self–attention and used 116 ROIs. The learning process was a 10–fold cross validation, batch size of 8, Adam [68] optimizer, learning rate of 0.01 and utilizing the cross entropy loss.

Latent Space Item Response Model (LSIRM)

LSIRM [14] is the model that regards item response structure dataset as a bipartite network and estimates the interaction between items and respondents. We set our goals to estimate the latent positions of ROI functions based on the interaction among patients. Since the original LSIRM is designed for item response dataset where each cell value is 0 or 1. However, we applies LSIRM to ROI–patient dataset where each cell value is continuous. Therefore, we adopt continuous version of LSIRM [15] to estimate the latent positions of ROI. Equation (2) shows the continuous version of LSIRM:

$$\mathbb{P}(y_{ji} \mid \boldsymbol{\Theta}) \sim \text{Normal}(\theta_j + \beta_i - ||\mathbf{u}_j - \mathbf{v}_i||, \sigma^2). \tag{2}$$

where, y_{ji} is probability of patient i reacts on ROI j. Each $\boldsymbol{\Theta}$ represents $\{\boldsymbol{\theta} = \{\theta_j\}, \boldsymbol{\beta} = \{\beta_i\}, \mathbf{U} = \{\mathbf{u_j}\}, \mathbf{V} = \{\mathbf{v_i}\}\}$ and $||\mathbf{u}_j - \mathbf{v}_i||$ represents the Euclidean distance between patient i and ROI j. LSRM consists of two parts; an attribute part and an interaction part. In attribute part, there are two parameters, $\theta_j \in \mathbb{R}$ and $\beta_i \in \mathbb{R}$, where β_i and θ_j represents that how many patients i reacts on ROI j. If the value of β_i is large then many ROI from patient i react and the value of θ_j is large it represents many patient react on j ROI. In an interaction part, there are latent configuration of patient i and ROI j, $\mathbf{u}_j$ and $\mathbf{v}_i$. With this latent positions, we can catch interactions between patient i and ROI j and visualize them in a Euclidean space. The shorter the distance between $\mathbf{u}_j$ and $\mathbf{v_i}$, the greater the probability that patient i reacts on ROI i. Additionally, if latent position for patient i and k, $\mathbf{u}_j$ and $\mathbf{u_k}$, are close ,then the patient i and k have similar reaction pattern.

To estimate parameters in LSIRM, we use Bayesian inference. We specify prior distribution for the parameters:

$$
\begin{aligned}
\beta_i | \tau_\beta^2 &\sim \text{N}(0, \tau_\beta^2), \quad \tau_\beta^2 > 0 \\
\theta_j | \sigma^2 &\sim \text{N}(0, \sigma_\theta^2), \quad \sigma^2 > 0 \\
\sigma^2 &\sim \text{Inv-Gamma}(a, b), \quad a_> 0, \quad b > 0 \\
\sigma_\theta^2 &\sim \text{Inv-Gamma}(a_\sigma, b_\sigma), \quad a_\sigma > 0, \quad b_\sigma > 0 \\
\mathbf{u_j} &\sim \text{MVN}_d(\mathbf{0}, \mathbf{I}_d) \\
\mathbf{v_i} &\sim \text{MVN}_d(\mathbf{0}, \mathbf{I}_d).
\end{aligned} \tag{3}
$$

where $\mathbf{0}$ is a d–vector of zeros and $\mathbf{I}_d$ is the $d \times d$ identify matrix. The posterior distribution of LSRM is proportional to

$$
\begin{aligned}
\pi(\boldsymbol{\Theta}, \sigma^2 \mid \mathbf{Y}) \propto &\prod_j \prod_i \mathbb{P}(y_{ji} \mid \boldsymbol{\Theta})^{y_{ji}} (1 - \mathbb{P}(y_{ji} \mid \boldsymbol{\Theta}))^{1-y_{ji}} \\
&\times \prod_j \pi(\theta_j \mid \sigma_\theta^2) \pi(\sigma_\theta^2) \prod_i \pi(\beta_i) \\
&\times \prod_j \pi(\mathbf{u_j}) \prod_\mathbf{i} \pi(\mathbf{v_i}) \pi(\sigma^2)
\end{aligned} \tag{4}
$$

Therefore, we could obtain latent positions of ROI $\mathbf{u_j}$ which represents the reactions pattern from patients. Since our main interest is to compare the different patterns of ROI from different disease group, we extract the latent positions of ROI $\mathbf{u_j}$ from each disease group and compare the difference among ROI by mapping on euclidean space R^2.

Metrics

Kullback–Leibler Divergence (KLD)

The KLD that measures the similarity between the two distributions $q(\theta)$ and $\pi(\theta \mid \mathbf{D})$ which is

$$
\begin{aligned}
\text{KLD}\Big(q(\theta) \mid\mid \pi(\theta \mid \mathbf{D})\Big) &= \int q(\theta) \log \frac{q(\theta)}{\pi(\theta \mid \mathbf{D})} d\theta \\
&= \int q(\theta) \log q(\theta) d\theta - \int q(\theta) \log \pi(\theta, \mathbf{D}) d\theta + \log \pi(\mathbf{D}) \\
&= -(\mathrm{E}_q[\log(\pi(\theta, \mathbf{D}))] - \mathrm{E}_q[\log q(\theta)]) + \log \pi(\mathbf{D}),
\end{aligned}
\tag{5}
$$

where θ is the parameter and $\mathbf{D}$ is the data set. Since $\log \pi(\mathbf{D})$ is not a function of model parameters, minimising the KLD is equivalent to maximizing $\mathrm{E}_q[\log(\pi(\theta, \mathbf{D}))] - \mathrm{E}_q[\log q(\theta)]$, the evidence lower bound (ELBO).

Coefficient of Variation(CV)

The CV is calculated by dividing the standard deviation by the mean. It is used to compare data with different measurement units. In other words, the variance is affected by the scale. Therefore, the scale is normalized by dividing the mean. The greater the relative difference, the greater the value of the coefficient of variation.

Acknowledgements

References

[1] Dong Wen, Zhenhao Wei, Yanhong Zhou, Guolin Li, Xu Zhang, and Wei Han. Deep learning methods to process fmri data and their application in the diagnosis of cognitive impairment: a brief overview and our opinion. *Frontiers in neuroinformatics*, 12:23, 2018.

[2] Simeon Spasov, Luca Passamonti, Andrea Duggento, Pietro Lio, Nicola Toschi, Alzheimer's Disease Neuroimaging Initiative, et al. A parameter-efficient deep learning approach to predict conversion from mild cognitive impairment to alzheimer's disease. *Neuroimage*, 189:276–287, 2019.

[3] Mingxia Liu, Daoqiang Zhang, and Dinggang Shen. Relationship induced multi-template learning for diagnosis of alzheimer's disease and mild cognitive impairment. *IEEE transactions on medical imaging*, 35(6):1463–1474, 2016.

[4] Ali Khazaee, Ata Ebrahimzadeh, and Abbas Babajani-Feremi. Application of advanced machine learning methods on resting-state fmri network for identification of mild cognitive impairment and alzheimer's disease. *Brain imaging and behavior*, 10(3):799–817, 2016.

[5] Yifat Brill-Karniely, Dvir Dror, Tal Duanis-Assaf, Yoel Goldstein, Ouri Schwob, Talya Millo, Natalie Orehov, Tal Stern, Mohammad Jaber, Netanel Loyfer, et al. Triangular correlation (trc) between cancer aggressiveness, cell uptake capability, and cell deformability. *Science advances*, 6(3):eaax2861, 2020.

[6] George H Dunteman. *Principal components analysis*. Number 69. Sage, 1989.

[7] Laurens Van der Maaten and Geoffrey Hinton. Visualizing data using t-sne. *Journal of machine learning research*, 9(11), 2008.

[8] Leland McInnes, John Healy, and James Melville. Umap: Uniform manifold approximation and projection for dimension reduction. *arXiv preprint arXiv:1802.03426*, 2018.

[9] Frédéric Chazal and Bertrand Michel. An introduction to topological data analysis: fundamental and practical aspects for data scientists. *arXiv preprint arXiv:1710.04019*, 2017.

[10] Shizhe Chen, Jia Chen, Qin Jin, and Alexander Hauptmann. Class-aware self-attention for audio event recognition. In *Proceedings of the 2018 ACM on International Conference on Multimedia Retrieval*, pages 28–36, 2018.

[11] Jie Zheng, Andi Xia, Lin Shao, Tao Wan, and Zengchang Qin. Stock volatility prediction based on self-attention networks with social information. In *2019 IEEE Conference on Computational Intelligence for Financial Engineering & Economics (CIFEr)*, pages 1–7. IEEE, 2019.

[12] Yongbin Sun, Yue Wang, Ziwei Liu, Joshua Siegel, and Sanjay Sarma. Pointgrow: Autoregressively learned point cloud generation with self-attention. In *Proceedings of the IEEE/CVF Winter Conference on Applications of Computer Vision*, pages 61–70, 2020.

[13] Dzmitry Bahdanau, Kyunghyun Cho, and Yoshua Bengio. Neural machine translation by jointly learning to align and translate. *arXiv preprint arXiv:1409.0473*, 2014.

[14] Minjeong Jeon, Ick Hoon Jin, Michael Schweinberger, and Samuel Baugh. Mapping unobserved item–respondent interactions: A latent space item response model with interaction map. *Psychometrika*, pages 1–26, 2021.

[15] Yeseul Jeon, Dongjun Chung, Jina Park, and Ick Hoon Jin. Network-based trajectory analysis of topic interaction map for text mining of covid-19 biomedical literature, 2021.

[16] Clifford R Jack Jr, Matt A Bernstein, Nick C Fox, Paul Thompson, Gene Alexander, Danielle Harvey, Bret Borowski, Paula J Britson, Jennifer L. Whitwell, Chadwick Ward, et al. The alzheimer's disease neuroimaging initiative (adni): Mri methods. *Journal of Magnetic Resonance Imaging: An Official Journal of the International Society for Magnetic Resonance in Medicine*, 27(4):685–691, 2008.

[17] Susanne G Mueller, Michael W Weiner, Leon J Thal, Ronald C Petersen, Clifford R Jack, William Jagust, John Q Trojanowski, Arthur W Toga, and Laurel Beckett. Ways toward an early diagnosis in alzheimer's disease: the alzheimer's disease neuroimaging initiative (adni). *Alzheimer's & Dementia*, 1(1):55–66, 2005.

[18] Nathalie Tzourio-Mazoyer, Brigitte Landeau, Dimitri Papathanassiou, Fabrice Crivello, Olivier Etard, Nicolas Delcroix, Bernard Mazoyer, and Marc Joliot. Automated anatomical labeling of activations in spm using a macroscopic anatomical parcellation of the mni mri single-subject brain. *Neuroimage*, 15(1):273–289, 2002.

[19] Manhua Liu, Fan Li, Hao Yan, Kundong Wang, Yixin Ma, Li Shen, Mingqing Xu, Alzheimer's Disease Neuroimaging Initiative, et al. A multi-model deep convolutional neural network for automatic hippocampus segmentation and classification in alzheimer's disease. *Neuroimage*, 208:116459, 2020.

[20] Chong-Yaw Wee, Chaoqiang Liu, Annie Lee, Joann S Poh, Hui Ji, Anqi Qiu, Alzheimers Disease Neuroimage Initiative, et al. Cortical graph neural network for ad and mci diagnosis and transfer learning across populations. *NeuroImage: Clinical*, 23:101929, 2019.

[21] Tianqi Chen and Carlos Guestrin. Xgboost: A scalable tree boosting system. In *Proceedings of the 22nd acm sigkdd international conference on knowledge discovery and data mining*, pages 785–794, 2016.

[22] Shangran Qiu, Prajakta S Joshi, Matthew I Miller, Chonghua Xue, Xiao Zhou, Cody Karjadi, Gary H Chang, Anant S Joshi, Brigid Dwyer, Shuhan Zhu, et al. Development and validation of an interpretable deep learning framework for alzheimer's disease classification. *Brain*, 143(6):1920–1933, 2020.

[23] Hasib Zunair, Aimon Rahman, Nabeel Mohammed, and Joseph Paul Cohen. Uniformizing techniques to process ct scans with 3d cnns for tuberculosis prediction. In *International Workshop on PRedictive Intelligence In MEdicine*, pages 156–168. Springer, 2020.

[24] Laura W de Jong, Karin van der Hiele, Ilya M Veer, JJ Houwing, RGJ Westendorp, ELEM Bollen, Paul W de Bruin, HAM Middelkoop, Mark A van Buchem, and Jeroen van der Grond. Strongly reduced volumes of putamen and thalamus in alzheimer's disease: an mri study. *Brain*, 131(12):3277–3285, 2008.

[25] Clifford R Jack, Ronald C Petersen, Yue Cheng Xu, Peter C O'Brien, Glenn E Smith, Robert J Ivnik, Bradley F Boeve, Stephen C Waring, Eric G Tangalos, and Emre Kokmen. Prediction of ad with mri-based hippocampal volume in mild cognitive impairment. *Neurology*, 52(7):1397–1397, 1999.

[26] Arnold Bakker, Gregory L Krauss, Marilyn S Albert, Caroline L Speck, Lauren R Jones, Craig E Stark, Michael A Yassa, Susan S Bassett, Amy L Shelton, and Michela Gallagher. Reduction of hippocampal hyperactivity improves cognition in amnestic mild cognitive impairment. *Neuron*, 74(3):467–474, 2012.

[27] Mario Manto and Peter Mariën. Schmahmann's syndrome-identification of the third cornerstone of clinical ataxiology. *Cerebellum & ataxias*, 2(1):1–5, 2015.

[28] Roberta M Kelly and Peter L Strick. Cerebellar loops with motor cortex and prefrontal cortex of a nonhuman primate. *Journal of neuroscience*, 23(23):8432–8444, 2003.

[29] Heidi IL Jacobs, David A Hopkins, Helen C Mayrhofer, Emiliano Bruner, Fred W van Leeuwen, Wijnand Raaijmakers, and Jeremy D Schmahmann. The cerebellum in alzheimer's disease: evaluating its role in cognitive decline. *Brain*, 141(1):37–47, 2018.

[30] Christine C Guo, Rachel Tan, John R Hodges, Xintao Hu, Saber Sami, and Michael Hornberger. Network-selective vulnerability of the human cerebellum to alzheimer's disease and frontotemporal dementia. *Brain*, 139(5):1527–1538, 2016.

[31] Nancy Kanwisher, Josh McDermott, and Marvin M Chun. The fusiform face area: a module in human extrastriate cortex specialized for face perception. *Journal of neuroscience*, 17(11):4302–4311, 1997.

[32] Suping Cai, Tao Chong, Yun Zhang, Jun Li, Karen M von Deneen, Junchan Ren, Minghao Dong, Liyu Huang, Alzheimer's Disease Neuroimaging Initiative, et al. Altered functional connectivity of fusiform gyrus in subjects with amnestic mild cognitive impairment: a resting-state fmri study. *Frontiers in human neuroscience*, 9:471, 2015.

[33] Rei Enatsu, Jorge Gonzalez-Martinez, Juan Bulacio, Yuichi Kubota, John Mosher, Richard C Burgess, Imad Najm, and Dileep R Nair. Connections of the limbic network: a corticocortical evoked potentials study. *Cortex*, 62:20–33, 2015.

[34] Basant K Puri, Philip M Jakeman, M Agour, KDR Gunatilake, KAC Fernando, AI Gurusinghe, IH Treasaden, AD Waldman, and P Gishen. Regional grey and white matter volumetric changes in myalgic encephalomyelitis (chronic fatigue syndrome): a voxel-based morphometry 3 t mri study. *The British journal of radiology*, 85(1015):e270–e273, 2012.

[35] Xia-an Bi, Qian Xu, Xianhao Luo, Qi Sun, and Zhigang Wang. Analysis of progression toward alzheimer's disease based on evolutionary weighted random support vector machine cluster. *Frontiers in neuroscience*, 12:716, 2018.

[36] Peipeng Liang, Jie Xiang, Hong Liang, Zhigang Qi, Kuncheng Li, Alzheimer's Disease NeuroImaging Initiative, et al. Altered amplitude of low-frequency fluctuations in early and late mild cognitive impairment and alzheimer's disease. *Current Alzheimer Research*, 11(4):389–398, 2014.

[37] Suping Cai, Liyu Huang, Jia Zou, Longlong Jing, Buzhong Zhai, Gongjun Ji, Karen M Von Deneen, Junchan Ren, Aifeng Ren, and Alzheimer's Disease Neuroimaging Initiative. Changes in thalamic connectivity in the early and late stages of amnestic mild cognitive impairment: a resting-state functional magnetic resonance study from adni. *PloS one*, 10(2):e0115573, 2015.

[38] Eek-Sung Lee, Kwangsun Yoo, Young-Beom Lee, Jinyong Chung, Ji-Eun Lim, Bora Yoon, and Yong Jeong. Default mode network functional connectivity in early and late mild cognitive impairment. *Alzheimer Disease & Associated Disorders*, 30(4):289–296, 2016.

[39] Eric M Reiman, Yakeel T Quiroz, Adam S Fleisher, Kewei Chen, Carlos Velez-Pardo, Marlene Jimenez-Del-Rio, Anne M Fagan, Aarti R Shah, Sergio Alvarez, Andrés Arbelaez, et al. Brain imaging and fluid biomarker analysis in young adults at genetic risk for autosomal dominant alzheimer's disease in the presenilin 1 e280a kindred: a case-control study. *The Lancet Neurology*, 11(12):1048–1056, 2012.

[40] Julia Spaniol, Patrick SR Davidson, Alice SN Kim, Hua Han, Morris Moscovitch, and Cheryl L Grady. Event-related fmri studies of episodic encoding and retrieval: meta-analyses using activation likelihood estimation. *Neuropsychologia*, 47(8-9):1765–1779, 2009.

[41] Scott A Small, Scott A Schobel, Richard B Buxton, Menno P Witter, and Carol A Barnes. A pathophysiological framework of hippocampal dysfunction in ageing and disease. *Nature Reviews Neuroscience*, 12(10):585–601, 2011.

[42] Xavier Delbeuck, Martial Van der Linden, and Fabienne Collette. Alzheimer'disease as a disconnection syndrome? *Neuropsychology review*, 13(2):79–92, 2003.

[43] J Patrick Kesslak, Orhan Nalcioglu, and Carl W Cotman. Quantification of magnetic resonance scans for hippocampal and parahippocampal atrophy in alzheimer's disease. *Neurology*, 41(1):51–51, 1991.

[44] Matthew Bobinski, MJ De Leon, J Wegiel, S Desanti, A Convit, LA Saint Louis, H Rusinek, and HM Wisniewski. The histological validation of post mortem magnetic resonance imaging-determined hippocampal volume in alzheimer's disease. *Neuroscience*, 95(3):721–725, 1999.

[45] Liana G Apostolova, Rebecca A Dutton, Ivo D Dinov, Kiralee M Hayashi, Arthur W Toga, Jeffrey L Cummings, and Paul M Thompson. Conversion of mild cognitive impairment to alzheimer disease predicted by hippocampal atrophy maps. *Archives of neurology*, 63(5):693–699, 2006.

[46] Ya-di Li, Hui-jin He, Hai-bo Dong, Xiao-yuan Feng, Guo-ming Xie, and Ling-jun Zhang. Discriminative analysis of early-stage alzheimer's disease and normal aging with automatic segmentation technique in subcortical gray matter structures: a multicenter in vivo mri volumetric and dti study. *Acta Radiologica*, 54(10):1191–1200, 2013.

[47] Wen-Zhen Zhu, Wei-de Zhong, Wei Wang, Chuan-jia Zhan, Cheng-yuan Wang, Jian-pin Qi, Jian-zhi Wang, and Ting Lei. Quantitative mr phase-corrected imaging to investigate increased brain iron deposition of patients with alzheimer disease. *Radiology*, 253(2):497–504, 2009.

[48] Takashi Yoshiura, Futoshi Mihara, Koji Ogomori, Atsuo Tanaka, Koichiro Kaneko, and Kouji Masuda. Diffusion tensor in posterior cingulate gyrus: correlation with cognitive decline in alzheimer's disease. *Neuroreport*, 13(17):2299–2302, 2002.

[49] Andreas Fellgiebel, Matthias J Müller, Paulo Wille, Paulo R Dellani, Armin Scheurich, Lutz G Schmidt, and Peter Stoeter. Color-coded diffusion-tensor-imaging of posterior cingulate fiber tracts in mild cognitive impairment. *Neurobiology of aging*, 26(8):1193–1198, 2005.

[50] KJCJ Kantarci, CR Jack, YC Xu, NG Campeau, PC O'Brien, GE Smith, RJ Ivnik, BF Boeve, E Kokmen, EG Tangalos, et al. Regional metabolic patterns in mild cognitive impairment and alzheimer's disease: a 1h mrs study. *Neurology*, 55(2):210–217, 2000.

[51] Stephen W Scheff and Douglas A Price. Alzheimer's disease-related synapse loss in the cingulate cortex. *Journal of Alzheimer's Disease*, 3(5):495–505, 2001.

[52] Gwénaëlle Catheline, Olivier Periot, Marion Amirault, Marc Braun, Jean-François Dartigues, Sophie Auriacombe, and Michèle Allard. Distinctive alterations of the cingulum bundle during aging and alzheimer's disease. *Neurobiology of aging*, 31(9):1582–1592, 2010.

[53] Yi-Cheng Lin, Yao-Chia Shih, Wen-Yih I Tseng, Yu-Hsiu Chu, Meng-Tien Wu, Ta-Fu Chen, Pei-Fang Tang, and Ming-Jang Chiu. Cingulum correlates of cognitive functions in patients with mild cognitive impairment and early alzheimer's disease: a diffusion spectrum imaging study. *Brain topography*, 27(3):393–402, 2014.

[54] Lele Xu, Xia Wu, Rui Li, Kewei Chen, Zhiying Long, Jiacai Zhang, Xiaojuan Guo, Li Yao, Alzheimer's Disease Neuroimaging Initiative, et al. Prediction of progressive mild cognitive impairment by multi-modal neuroimaging biomarkers. *Journal of Alzheimer's Disease*, 51(4):1045–1056, 2016.

[55] Marcos Domic-Siede, Martín Irani, Joaquín Valdés, Marcela Perrone-Bertolotti, and Tomás Ossandón. Theta activity from frontopolar cortex, mid-cingulate cortex and anterior cingulate cortex shows different roles in cognitive planning performance. *NeuroImage*, 226:117557, 2021.

[56] James F Cavanagh and Michael J Frank. Frontal theta as a mechanism for cognitive control. *Trends in cognitive sciences*, 18(8):414–421, 2014.

[57] Dingailu Ma, Irfete S Fetahu, Mei Wang, Rui Fang, Jiahui Li, Hang Liu, Tobin Gramyk, Isabella Iwanicki, Sophie Gu, Winnie Xu, et al. The fusiform gyrus exhibits an epigenetic signature for alzheimer's disease. *Clinical epigenetics*, 12(1):1–16, 2020.

[58] Lulu Zhang, Huangjing Ni, Zhinan Yu, Jun Wang, Jiaolong Qin, Fengzhen Hou, Albert Yang, Alzheimer's Disease Neuroimaging Initiative (ADNI, et al. Investigation on the alteration of brain functional network and its role in the identification of mild cognitive impairment. *Frontiers in neuroscience*, 14:1027, 2020.

[59] Jeremy D Schmahmann, Carl M Anderson, Natika Newton, and Ralph D Ellis. The function of the cerebellum in cognition, affect and consciousness: Empirical support for the embodied mind. *Consciousness & emotion*, 2(2):273–309, 2001.

[60] Neelum T Aggarwal, Robert S Wilson, Todd L Beck, Julia L Bienias, and David A Bennett. Motor dysfunction in mild cognitive impairment and the risk of incident alzheimer disease. *Archives of neurology*, 63(12):1763–1769, 2006.

[61] Jeremy D Schmahmann and Janet C Sherman. The cerebellar cognitive affective syndrome. *Brain: a journal of neurology*, 121(4):561–579, 1998.

[62] Jennifer L Whitwell, Stephen D Weigand, Bradley F Boeve, Matthew L Senjem, Jeffrey L Gunter, Mariely DeJesus-Hernandez, Nicola J Rutherford, Matthew Baker, David S Knopman, Zbigniew K Wszolek, et al. Neuroimaging signatures of frontotemporal dementia genetics: C9orf72, tau, progranulin and sporadics. *Brain*, 135(3):794–806, 2012.

[63] Jeremy D Schmahmann. Dysmetria of thought: clinical consequences of cerebellar dysfunction on cognition and affect. *Trends in cognitive sciences*, 2(9):362–371, 1998.

[64] Jeremy D Schmahmann, Jeffrey B Weilburg, and Janet C Sherman. The neuropsychiatry of the cerebellum—insights from the clinic. *The cerebellum*, 6(3):254–267, 2007.

[65] G Russo, DS Sardina, P Alongi, R Coppola, V Puglisi, A Stefano, R Giugno, LM Grimaldi, S Scalisi, M Midiri, et al. 79. amyloid-pet analysis based on tissue probability maps. *Physica Medica: European Journal of Medical Physics*, 56:111–112, 2018.

[66] Zhiqun Wang, Chaogan Yan, Cheng Zhao, Zhigang Qi, Weidong Zhou, Jie Lu, Yong He, and Kuncheng Li. Spatial patterns of intrinsic brain activity in mild cognitive impairment and alzheimer's disease: A resting-state functional mri study. *Human brain mapping*, 32(10):1720–1740, 2011.

[67] Jungho Cha, Jung-Min Hwang, Hang Joon Jo, Sang Won Seo, Duk L Na, and Jong-Min Lee. Assessment of functional characteristics of amnestic mild cognitive impairment and alzheimer's disease using various methods of resting-state fmri analysis. *BioMed research international*, 2015, 2015.

[68] Diederik P Kingma and Jimmy Ba. Adam: A method for stochastic optimization. *arXiv preprint arXiv:1412.6980*, 2014.
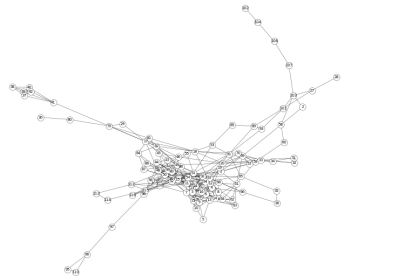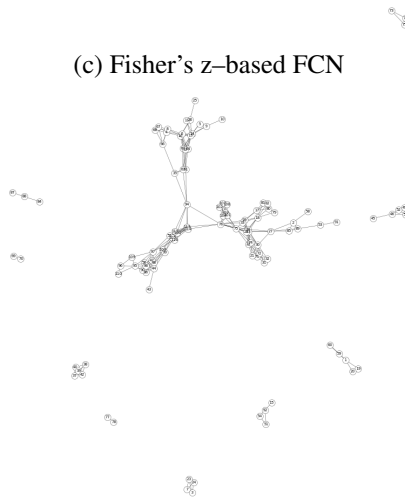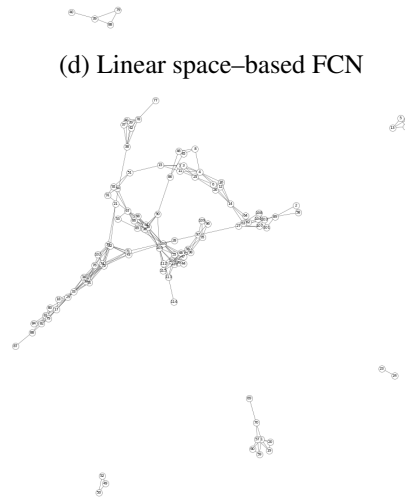
A Functional Connectivity Network
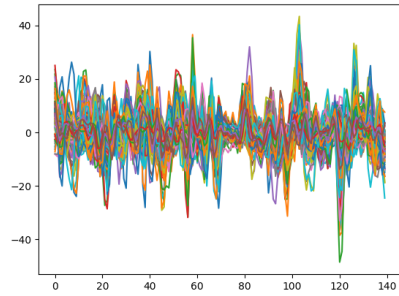

(a) rs–fMRI BOLD signal
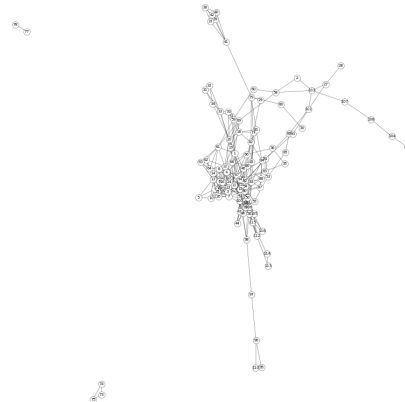
(b) Pearson's r–based FCN

(c) Fisher's z–based FCN

(d) Linear space–based FCN

(e) Stochastic space–based FCN

(f) Topological space–based FCN

Figure 8: Correlation coefficient–based FCN and latent space–based FCN of AD patient
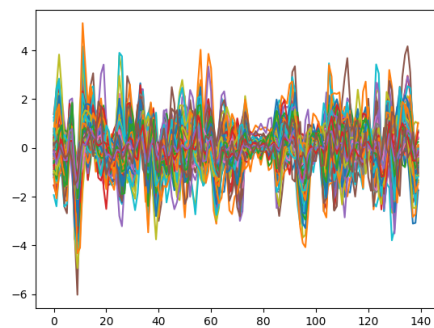
(a) rs–fMRI BOLD signal
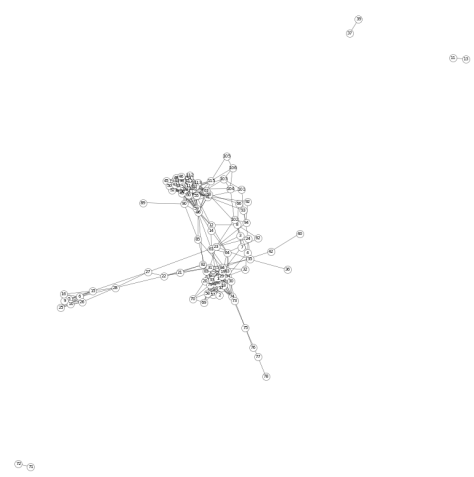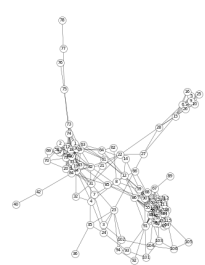
(b) Pearson's r–based FCN

(c) Fisher's z–based FCN
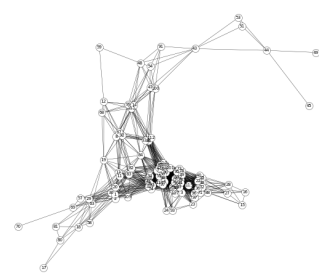
(d) Linear space–based FCN
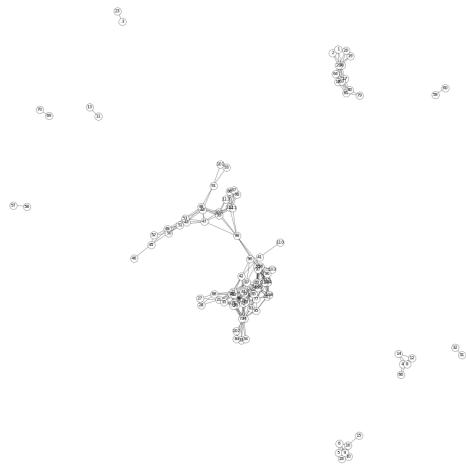
(e) Stochastic space–based FCN

(f) Topological space–based FCN

Figure 9: Correlation coefficient–based FCN and latent space–based FCN of MCI patient
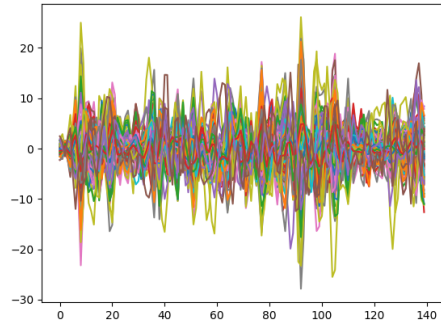
(a) rs–fMRI BOLD signal
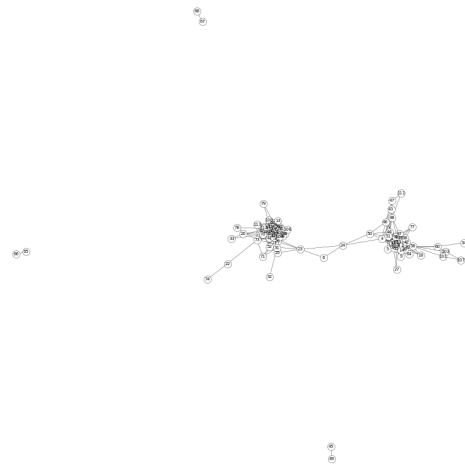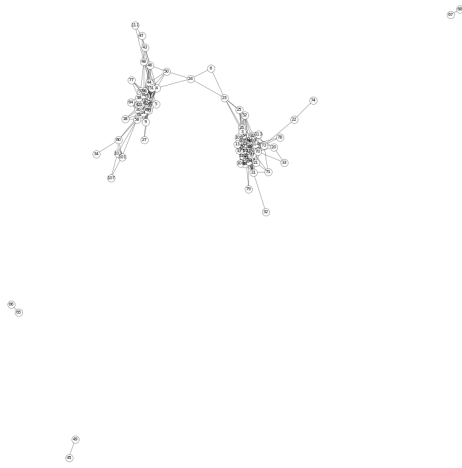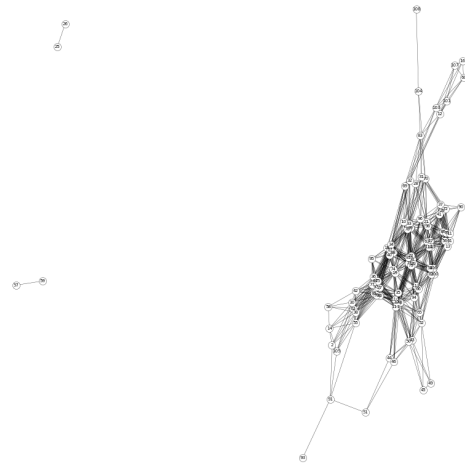
(b) Pearson's r–based FCN

(c) Fisher's z–based FCN

(d) Linear space–based FCN
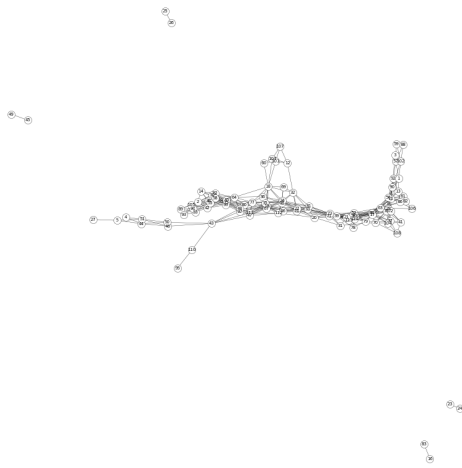
(e) Stochastic space–based FCN
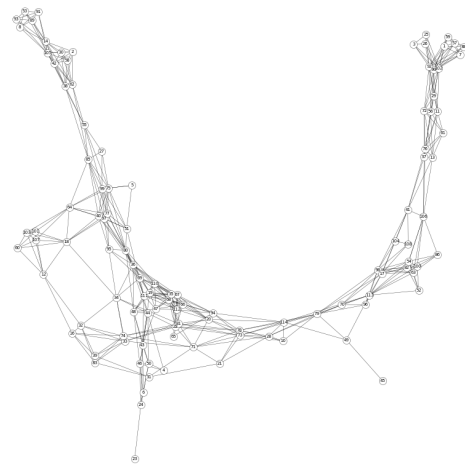
(f) Topological space–based FCN

Figure 10: Correlation coefficient–based FCN and latent space–based FCN of EMCI patient
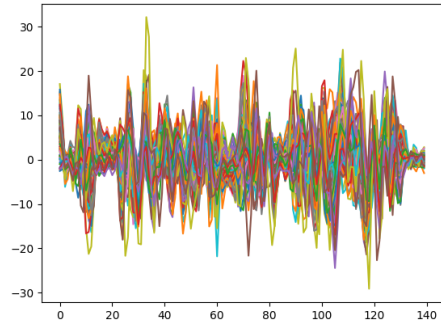
(a) rs–fMRI BOLD signal
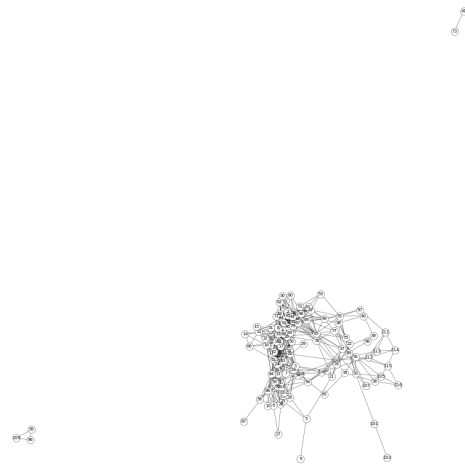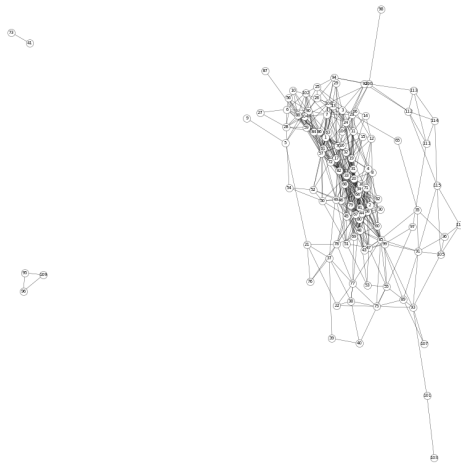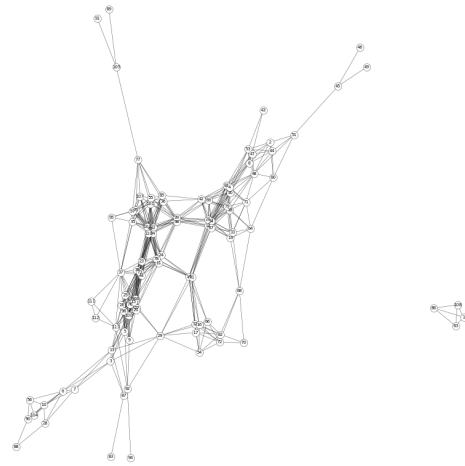
(b) Pearson's r–based FCN

(c) Fisher's z–based FCN

(d) Linear space–based FCN

(e) Stochastic space–based FCN
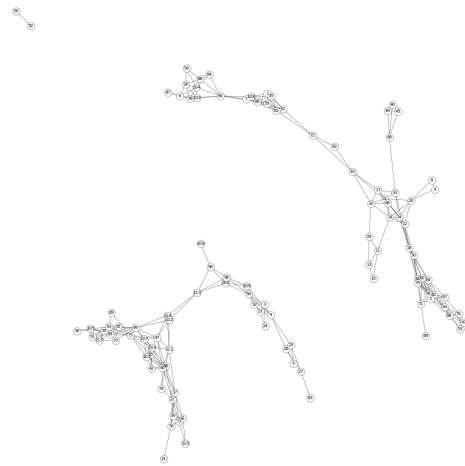
(f) Topological space–based FCN

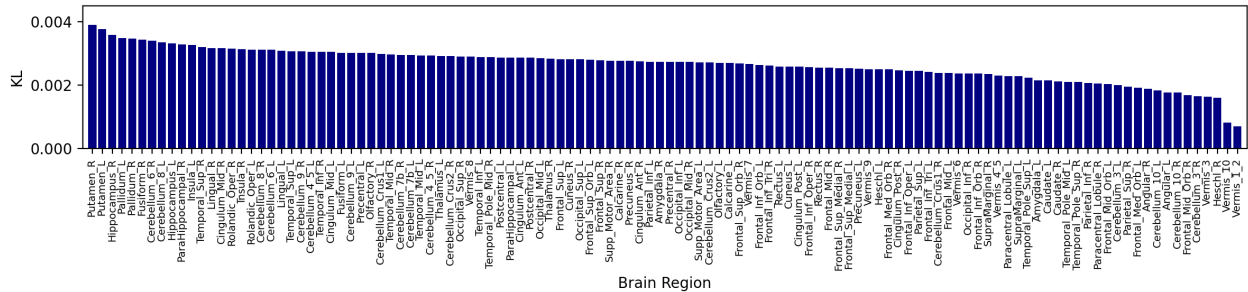Figure 11: Correlation coefficient–based FCN and latent space–based FCN of LMCI patient

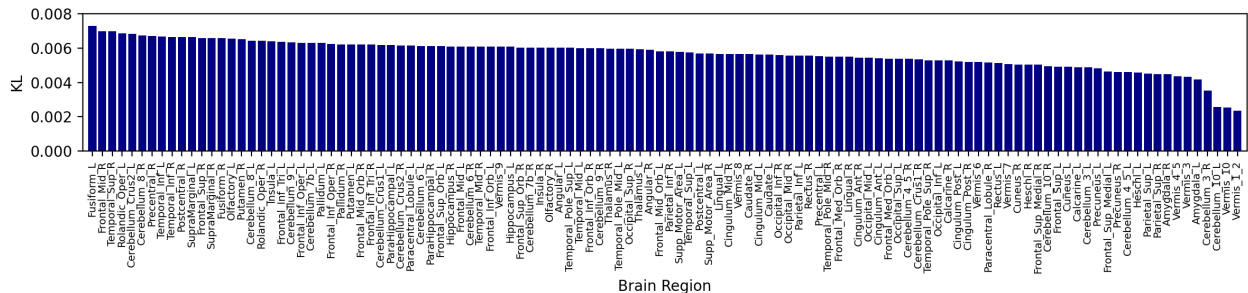# B Kullback–Leibler Divergence value for compared diseases' group
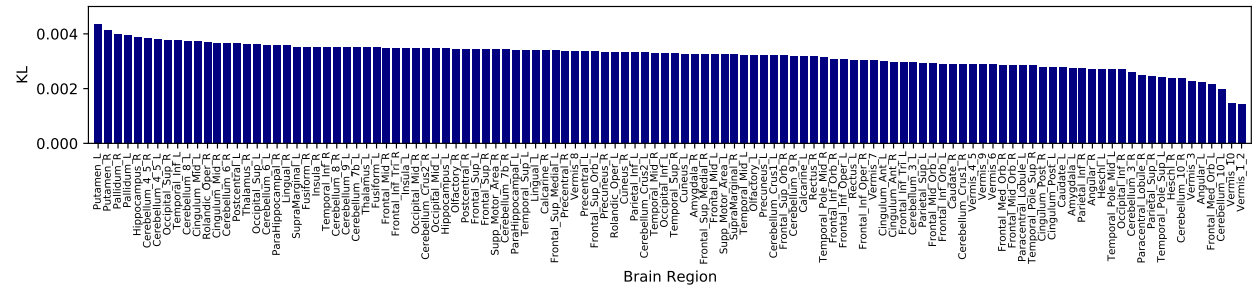
(a) AD vs MCI
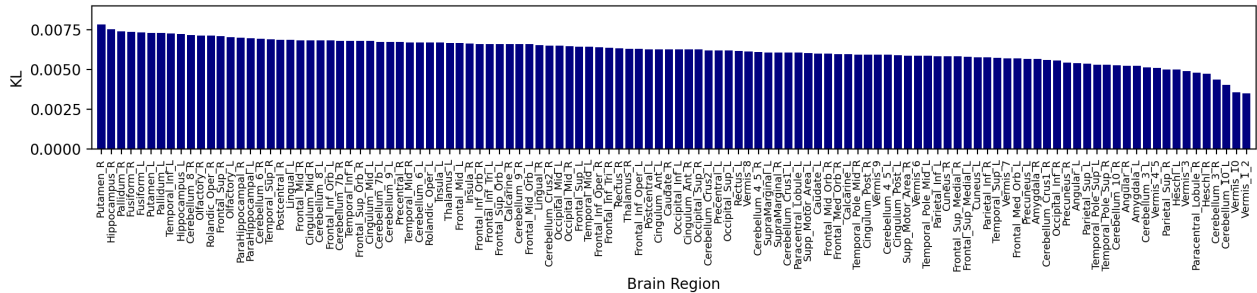
(b) AD vs EMCI

(c) AD vs LMCI

(d) EMCI vs LMCI

Figure 12: Kullback–Leibler Divergence value for compared diseases' group